Sedimentary Geology 444 (2023) 106313

Contents lists available at ScienceDirect

Sedimentary Geology

journal homepage: www.elsevier.com/locate/sedgeo

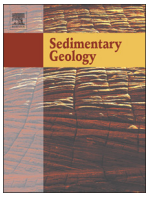

Comparative geochemistry of Early Carboniferous marine red beds (MRBs) and their significance for deep time paleoceanographic reconstructions

Christopher J. Card [a], Michael Montenari [b,*]

[a] Department of Geology and Geophysics, University of Aberdeen, Aberdeen AB24 3UE, UK
[b] Geography, Geology and the Environment, Keele University, Keele ST5 5BG, UK

ARTICLE INFO

Article history:
Received 21 September 2022
Received in revised form 29 November 2022
Accepted 30 November 2022
Available online 9 December 2022

Editor: Dr. Catherine Chagué

Keywords:
Marine red beds
Geochemistry
Viséan
Oceanic red beds
Paleotethys
Balearic Islands

ABSTRACT

Marine red beds (MRBs), also known as oceanic red beds (ORBs), are reddish colored sediments deposited within the marine realm that have been stained during deposition and/or early diagenesis because of changes in the ocean water chemistry in response to paleoceanographic and paleoclimatological factors. Although common throughout the Phanerozoic, marine red beds have mostly been investigated in Upper Cretaceous successions as CORBs (Cretaceous Oceanic Red Beds) - their occurrence and paleoceanographic context within the Paleozoic has yet to be studied in detail. Here we describe and interpret the high-resolution litho- and chemofacies of Early Carboniferous (Late Viséan) marine red beds from the northern coast of Menorca (Balearic Islands, Spain) that mark a rapid transition from siliceous radiolarian chert deposition to re-worked carbonate debrites followed by typical European Culm facies. The succession was deposited within a strait-like narrow basin that formed part of the Alboran-Kabylian-Peloritan-Calabrian terrane in the Western Paleotethys Ocean prior to the onset of the Variscan Orogeny. The marine red bed geochemistry is described in terms of three geochemical endmembers Al-MRBs (clayey), Ca-MRBs (calcareous) and Si-MRBs (siliceous) by using XRF-derived Al_2O_3, CaO, and SiO_2 concentrations. This study finds that Viséan marine red beds from Menorca are predominantly Al-MRBs with subordinate Ca-MRBs. Furthermore, we compare the bulk rock geochemistry of the Viséan marine red beds of this study with the geochemical data of Paleozoic, Mesozoic and Cenozoic marine red beds available in the existing literature (Cambrian, Silurian, Jurassic, Cretaceous, Paleogene and recent Pacific Ocean red clays) to highlight the significance of marine red bed occurrences in relation to (paleo-)bioproductivity fluctuations, deep-water oxygenation and oceanic redox transitions. This study finds that Phanerozoic marine red beds are dominantly Al-MRBs and Ca-MRBs, whilst Si-MRBs are less common. The Early Carboniferous marine red beds of the present study were formed in a distal, deeper-marine environment under oxic-suboxic, oligotrophic conditions. A lack of any significant Fe_2O_3T enrichment points towards a more complex diagenetic process for the origin of the red color imparted in Phanerozoic MRBs.

1. Introduction

Red beds, also commonly known as continental red beds (CRBs), are globally widespread sedimentary successions depicting an overall reddish-color (red/pink/brown) and are traditionally seen as a reliable indicator for terrestrial deposition under oxidizing conditions (Turner, 1980; Tucker, 2003).

The occurrences of reddish-colored deposits in the marine realm are usually described as marine red beds (MRBs). MRBs can refer to a range of different marine-deposited lithologies that developed in shallow-water to ultra-deep (below CCD) environments throughout the geological record (Wagreich et al., 2009), as well as in modern oceans, notably the Pacific (Clauer et al., 1982; Bryant and Bennet, 1988; Glasby, 1991). In general, the lithologies more commonly associated with MRBs are limestones, clays, shales, and calcareous mudstones (Hu et al., 2005). MRBs have been subdivided into three broad categories based upon the water depth of deposition and are considered as so-called time-specific facies (Brett et al., 2012; Rong et al., 2012): [Type-I] Oceanic-type marine red beds, also described as oceanic red beds (ORBs) or deep oceanic red beds (DORBs), considered to be deposited under oligotrophic, oxic to sub-oxic conditions in pelagic and hemipelagic environments (Hu et al., 2005; Wang et al., 2009). [Type-II] Deeper-water-type marine red beds deposited in offshore to ramp margin environments (Ziegler and

* Corresponding author.
E-mail address: m.montenari@keele.ac.uk (M. Montenari).

https://doi.org/10.1016/j.sedgeo.2022.106313

McKerrow, 1975; Luan et al., 2019). [Type-III] Shallow-water-type marine red beds deposited in near-shore basins and along inner shelf environments (Rong et al., 2012; Zhang et al., 2014; Liu et al., 2016). The latter two are more strongly controlled by changes of the regional and local paleoenvironmental conditions as well as sediment supply. They often gain their red color from the fluvial input of oxidized detrital hinterland material and are therefore not necessarily reflective of deep ocean oxygenation and/or Fe-rich oceans (Zhang et al., 2014; Song et al., 2017). However, it must be noted that the deposition of deeper-water and shelf margin MRBs was recently linked to transgressive events enabling ocean ventilation and subsequent oxygenation of sediments across platforms as described and interpreted from the Early–Middle Ordovician Zitai Formation along the Yangtze Platform (Luan et al., 2019). Principally, deep marine sediments deposited under pelagic to hemipelagic conditions are most likely to record and reflect large scale paleoenvironmental changes as they are less susceptible to seasonal and regional cyclicity (Wagreich et al., 2009; Song et al., 2017). The defining component for the red coloration in type-I and some type-II MRBs is considered to originate from homogenously dispersed diagenetic hematite nano-grains which form by the oxidation of iron on the seabed and during shallow burial (Franke and Paul, 1980; Torrent and Schwertmann, 1987; Eren and Kadir, 1999; Wang et al., 2005; Cai et al., 2009; Cai et al., 2012). To enable diagenetic hematite formation sustained oxygenated conditions across the sediment-water interface and slow sediment accumulation rates are required (Wagreich and Krenmayr, 2005; Jansa and Hu, 2009). The red coloration in red shales is thought to be solely associated with hematite (blood red; 3.5R–4.1YR, Munsell hue), whereas in red limestones goethite (bright yellow; 8.1YR–1.6Y, Munsell hue) and Mn^{2+}-bearing calcite (red tinge) are also considered to impart a red color (Torrent and Schwertmann, 1987; Cai et al., 2008; Cai et al., 2009; Li et al., 2011; Hu et al., 2012).

Over the past 15 years the number of MRB studies has progressively increased, as the importance of MRBs as markers for paleoceanographic changes during the evolution of ancient marine environments is becoming more recognized (Brett et al., 2012; Luan et al., 2021). This includes their potential temporal linkage to periods following prevailing oceanic anoxia notable throughout the Phanerozoic (Yilmaz, 2008; Hu et al., 2012; Song et al., 2017). Prior to the recent advancements in our understanding of MRBs, only a limited number of MRB studies were available, largely due to the highly diachronous nature and relatively sparse or unknown occurrence of MRB-bearing successions throughout the geological record (Gümbel, 1861; Lajoie and Chagnon, 1973; Ziegler and McKerrow, 1975; Arthur and Fischer, 1977; Premoli Silva et al., 1989; Wagreich and Krenmayr, 2005). The apparent connection between MRBs and large scale climatic and paleoceanographic changes has resulted in a renewed scientific interest with many previously described examples being revisited, investigated, and interpreted (Herm, 1962; Wagreich, 1992; Wagreich and Krenmayr, 1993, 2005; Krenmayr, 1996; Hu et al., 2006; Neuhuber and Wagreich, 2009; Song et al., 2017).

Currently MRBs have been extensively studied within the Cretaceous (Cretaceous oceanic red beds - CORBs), defined by Hu et al. (2005) as red to pink to brown fine-grained sedimentary rocks of Cretaceous age deposited in hemipelagic and pelagic environments (Wang et al., 2004; Melinte and Jipa, 2005; Wang et al., 2005; Neuhuber et al., 2007; Skupien et al., 2009; Scott, 2009; Chen et al., 2011; Li et al., 2011). Investigations into CORB deposits have significantly furthered the current understanding of MRB distribution as well as their depositional mechanisms, identifying two dominant cycles: [1] Short-term CORB-cycles typically with a duration of <1 myr, and [2] long-term CORB-cycles with a duration of >4 myr that appear to be composed of multiple short-term CORB cycles (Scott, 2009; Hu et al., 2012). But the occurrence of MRBs is also established for other specific stratigraphic parts of the Phanerozoic. This was demonstrated by Song et al. (2017), who describe distinct phases of MRB deposition from five Phanerozoic periods (Cambrian, Devonian, Triassic, Jurassic, and Cretaceous). Furthermore, MRBs related to periods of oceanic anoxia such as the Mid-Late Ordovician (Bábek et al., 2021a; Degtyarev et al., 2021; Liu et al., 2021) and the Early Triassic (Baud, 2013; Li et al., 2019) have been reported. There is an increasing number of detailed geochemical studies that describe, characterize and interpret Phanerozoic MRBs aside from the Cretaceous (Lajoie and Chagnon, 1973; Kiipli et al., 2000; Bábek et al., 2018, 2021a, 2021b), although notably for the Carboniferous they are lacking. Here we present the major and minor element geochemistry of a late Viséan Paleotethyan succession of type-1 MRBs that is composed of mudstones, calcareous mudstones, and pelagic limestones from the northern coast of Menorca (Balearic Islands, Spain). This succession is described, characterized and interpreted utilizing Wagreich et al.'s (2009) and Hu et al.'s (2012) geochemical classification scheme for CORBs (Fig. 1).

Early Carboniferous MRBs have yet to be investigated in detail and have been unacknowledged in the wider context of global MRB studies. This paper aims to describe, compare, and interpret the chemofacies of Early Carboniferous MRBs from the Western Paleotethyan Ocean nowadays preserved on the Balearic Island of Menorca. It aims to consider the nature and significance of Early Carboniferous MRBs with regards to the paleoenvironmental and paleoceanographic conditions that prevailed in the Western Paleotethys Ocean and enabled their formation. To achieve this, high-resolution sedimentological and X-ray fluorescence spectrometry (XRF) geochemical data were generated, analyzed and interpreted to describe the marine red bed-specific chemofacies, thus enabling the comparison of the Early Carboniferous MRB geochemistry to the geochemistry of MRB occurrences throughout the Phanerozoic.

2. Geologic and geographic setting

The Balearic Islands are an archipelago and autonomous community of Spain that is situated in the western Mediterranean Sea approximately 150 km to the east of the Iberian Peninsula (Fig. 2A) and is constituted of the four larger islands of Mallorca, Menorca, Ibiza (Eivissa) and Formentera as well as several smaller islands and inlets. The Balearic Islands predominantly display a Triassic to Upper Miocene succession, with Menorca being the only island hosting Paleozoic strata (Bourrouilh, 1973, 1983), apart from contentious reports of a minor Early Carboniferous outcrop in the center of Mallorca (Rodríguez-Perea and Ramos-Guerrero, 1984).

Menorca depicts two dominant structural regimes as two physiographic regions: [1] the Tramuntana to the north that contains low-angled thrust sheets with pre-Alpine Paleozoic to Mesozoic strata trending NNW-SSE and [2] the Migjorn to the south, which comprises sub-horizontal post-Alpine Upper Miocene carbonates (Gelabert et al., 2005). These two regions are separated by a large-scale, Upper Miocene ESE-WNW trending and SSW dipping normal fault, which downfaults the Migjorn against the uplifted Tramuntana region (Fig. 2B).

2.1. Stratigraphy

Menorca is still lacking formal lithostratigraphic subdivisions. There are some informally designated units and stratigraphic numbering schemes available, that have been utilized in the past, mainly for the Permo-Triassic (Rosell et al., 1988; Gómez-Gras and Alonso-Zarza, 2003; Linol et al., 2009) and the Miocene (Freeman et al., 1989; Pomar et al., 2002), but also for correlations to lithostratigraphic units elsewhere in Europe (Herbig and Mamet, 1985; Herbig, 1985). Bourrouilh (1973, 1983) provided the main foundations to the current geological understanding of Menorca. It is generally assumed that Menorca is more closely associated with the internal zone of the Betic range (the Malaguides) rather than the external zone which includes the remaining Balearic Islands (Hollister, 1934; Fallot, 1948; Azema et al., 1974; Bourrouilh and Gorsline, 1979; Sàbat et al., 2018).

The Paleozoic succession exposed on Menorca is Early Devonian to Permian in age and has a non-metamorphic aspect in contrast to most of the low-grade, Alpine altered Paleozoic successions within the Betic

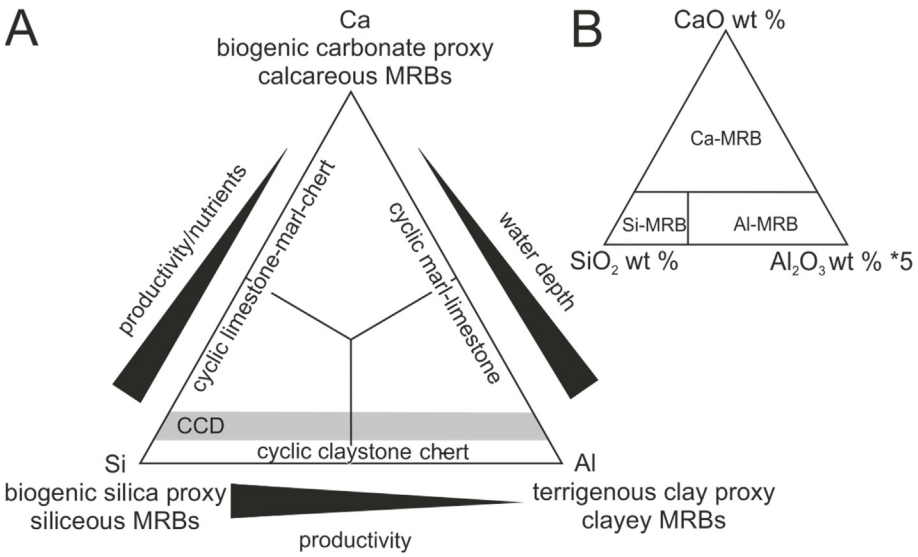

Fig. 1. Al-Ca-Si ternary diagram on the geochemical classification and major controlling factors for sedimentation of marine red beds (MRBs) into three endmembers of Al-MRBs (clayey), Ca-MRBs (calcareous) and Si-MRBs (siliceous) by Al_2O_3, CaO and SiO_2 values. Adapted from Wagreich et al.'s (2009) classification of Cretaceous oceanic red beds (CORBs) system (A) and Hu et al.'s (2012) geochemical classification of CORBs (B). (For interpretation of the references to color in this figure legend, the reader is referred to the web version of this article.)

Cordillera (Cruz and Andreo, 1997; Bourrouilh, 2016). The Devonian succession is estimated to be 1000 m thick and comprises of flysch facies from distal siliciclastic turbidite fan lobes underlain by black shale deposits considered to be Lochkovian in age (Bourrouilh, 1983; Rosell and Elizaga, 1989; Sàbat et al., 2018). The Carboniferous succession is estimated to be >3000 m in thickness and can be subdivided into the two informal units of [1] Tournaisian to Early Viséan siliciclastic and calcareous turbidites and [2] Late Viséan to Early Bashkirian radiolarian cherts and marine red beds followed by concordant 'Culm' facies from mid-fan-type environments (Bourrouilh, 1973; Bourrouilh and Termier, 1973; Orr, 1994; Orr et al., 1996; Hahn et al., 1997; Sàbat et al., 2018). The boundary between the two units is locally defined by the 'Nivel Olistostrómico', a limestone olistostrome approximately 50 m in thickness (Bourrouilh, 1973).

The site investigated for the present study is situated along the northern coast of Menorca (approximately 5.5 km west of Fornells) within the Es Mercadal municipal (Fig. 2C). The Early Carboniferous succession preserved within this region dips 18–22° towards the west and is thrusted on top of Permian strata. Generally, the Early Carboniferous succession is faulted and folded as a result of Variscan and Alpine tectonics, but also displays *syn*-sedimentary slump fold structures prominently within the radiolarian cherts in relation to the Nivel Olistostrómico.

The succession is described in greater detail by Bourrouilh and Termier (1973) who were able to assign eight informal lithostratigraphic units: [1]

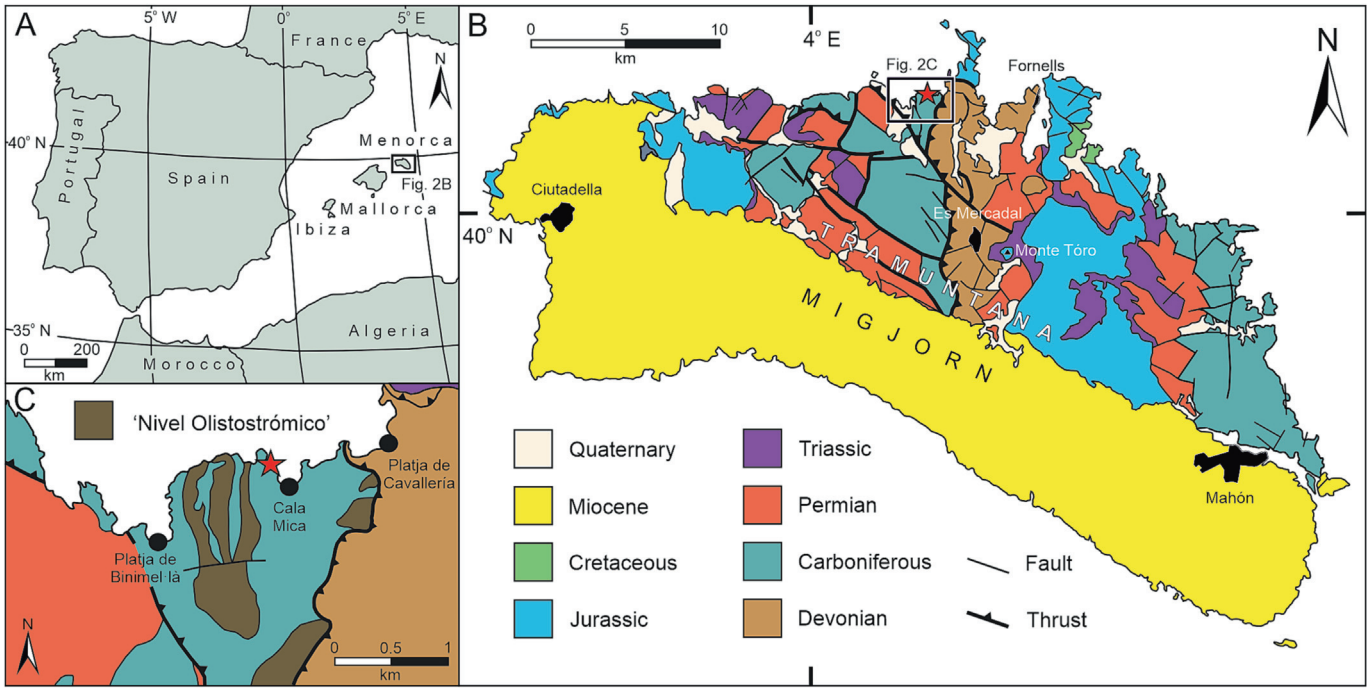

Fig. 2. (A) Regional map of the Western Mediterranean with the Island of Menorca highlighted (box). (B) Geological map of Menorca with study area and site highlighted (box and red star, respectively) within the Early Carboniferous to the north of the municipal of Es Mercadal (modified after Bourrouilh, 1983; Linol et al., 2009). (C) Geological map of study area with site of investigation highlighted (red star), located to the western side of Cala Mica at Punta d'en Valent (modified after Bourrouilh, 1983). (For interpretation of the references to color in this figure legend, the reader is referred to the web version of this article.)

10 m of white and green mudstones that are faulted and rest conformably on top of uppermost Devonian flysch facies. This unit represents the continuation of white and green mudstones of Ferragut Vell located to the immediate south-west of Platja de Cavalleria within the hanging wall of the thrust sheet to the east (Bourrouilh, 1983). [2] 10–15 m of thinly bedded green radiolarian cherts intercalated with green mudstones. [3] 2 m of black carbonaceous mudstones with phosphate nodules. [4] 20 m of dark radiolarites separated by thin horizons of black mudstone often with phosphate nodule levels. [5] 10–12 m of brecciated gray limestones interbedded with red mudstone, red siltstone, and red limestone, often with reduced/bleached green and yellow horizons. This particular level is dated as Viséan 3b via the crinoid species *Balearocrinus breimeri* (Bourrouilh and Termier, 1973) and the trilobite species *Drevermannia calamicensis* together with the goniatite species *Goniatites spirifer* and *Prionoceras latecostatum* (Nicolaus, 1963; Korn, 1996; Hahn et al., 1997). [6] 10 m of Culm facies graywackes and siltstones. [7] 10 m of red and yellow mudstones and siltstones with thin bioturbated sandstone beds. This level is dated as Viséan 3c by the occurrence of *Goniatites* cf. *striatus* (Bourrouilh and Termier, 1973), and marks the onset of more diverse faunal assemblages containing the bivalve genera *Posidonomya* and *Posidoniella* (Hollister, 1934). [8] This final unit represents a continued sedimentation of Culm facies graywackes and siltstones.

This study focuses upon the MRBs from Bourrouilh and Termier's (1973) unit [5], which documents the transition from dominantly radiolarian chert deposition to marine red bed deposition within the Cala Mica succession (see Fig. 3).

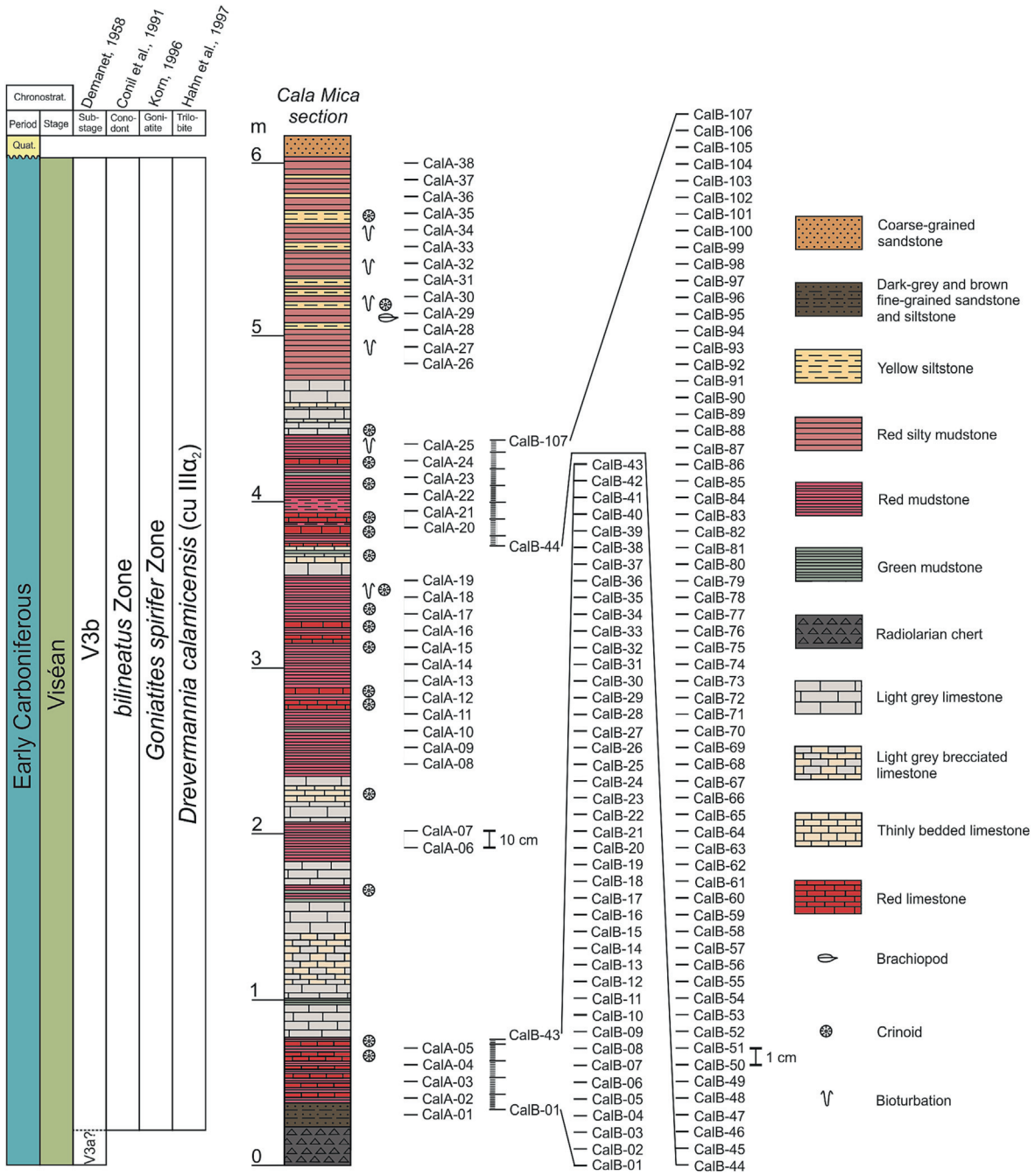

Fig. 3. Lithological log of the Cala Mica section located to the north of the Es Mercadal municipal on Menorca (Balearic Islands, Spain). Biostratigraphic age constraints are based upon data by Demanet (1958), Bourrouilh and Termier (1973), Conil et al. (1991), Korn (1996), and Hahn et al. (1997). Positions of samples gathered from the section for elemental analysis are given alongside the lithological log.

2.2. Paleogeographic framework

The late Paleozoic paleogeographic setting of the Western Mediterranean is complex and still largely not well understood.

The Paleozoic succession of Menorca has been compared and correlated in terms of lithostratigraphy and biostratigraphy to several contemporaneous successions of different Variscan massifs of the Western-Mediterranean to decipher and constrain the paleogeographical- and provenance relationships within the Western Paleotethys. These correlations were undertaken using the lithological similarities and differences of the clasts contained within distinct conglomeratic horizons. Two main conglomeratic levels have been established within the Early Carboniferous on Menorca (Flügel and Herbig, 1988): [1] Lower Serpukhovian limestone conglomerates containing Upper Devonian (lower *asymmetricas* to lower *gigas* and lower *marginifera* Zones) clasts preserved within the eastern thrust sheet at Cala des Murtar, located to the north of Mahon (Buchroithner et al., 1980a), are considered to be time-equivalent with the Ratamares Member of the Almogia Formation from the Malaguides (Buchroithner et al., 1980b; Herbig, 1985). [2] Lower Bashkirian limestone conglomerates and debrites at Binifaillet (located within the central thrust sheet, 1 km southwest of Es Mercadal) are also found in the Marbella Formation that stratigraphically overlies the Almogia Formation in the Malaguides (Herbig and Mamet, 1985). Furthermore, horizons considered to be equivalent to the ones described above were also documented from the Akaili- and Beni-Hozmar thrusts in the Moroccan Ghomaridic nappes (Bourrouilh and Lys, 1977; Flügel and Herbig, 1988). Herbig and Stattegger (1989) suggest that such 'conglomerate events' indicate episodical sediment transport across the Alpujárride and Malaguide realms (Alboran domain) from the Betico-rif block into the Menorcan realm (Bourrouilh and Lys, 1977; Flügel and Herbig, 1988; Herbig, 1989). The Early Carboniferous of Menorca displays genetically the most similar sedimentological characteristics of the Chenoua massif in Algeria and the Khudiat Tizan internal rif of the Moroccan nappes (Bourrouilh, 2016).

These depositional realms are considered to be part of the Alboran-Kabylian-Peloritan-Calabrian terrane or microcontinent (Dercourt et al., 1985; Bouillin et al., 1986), thought to have existed between the closing of the Rheic- and Paleotethys Oceans prior to the onset of the Variscan Orogeny and are nowadays preserved in the Khudiat Tizan (Morocco), Chenoua and Kabylies mountains (Algeria). Sediment supply is interpreted to have originated from the peri-Gondwanan Betico-Rif block, with Menorca located towards the north, closest to the Central Iberian chain (Herbig, 1989; Bourrouilh, 2016).

3. Methods

3.1. Sampling techniques

The samples used for lithological and elemental analysis were collected from the MRB facies of the Cala Mica section (Fig. 3). Samples were extracted at two different sampling resolutions. [1] A sampling interval systematically every 10 cm (see Fig. 3, CalA) throughout the entire succession yielded a low-resolution dataset of 38 MRB samples. [2] A sampling interval every 1 cm (see Fig. 3, CalB) throughout the first and fourth MRB units in the succession yielding high-resolution datasets of 43 and 64 MRB samples, respectively.

3.2. Marine red bed characterization

3.2.1. Facies analysis and petrography

Thin sections were prepared following standard practices, using selected MRB samples that were representative of each lithofacies. A Nikon Eclipse™ LV100N POL microscope equipped with a digital sight DS-Fi2 camera was used to describe, characterize and interpret the lithofacies as well as to generate photomicrographs. The different lithofacies types have been assigned based primarily upon color, lithology, texture, and biogenic content.

3.2.2. Elemental analysis

A Niton™ XL3t energy-dispersive X-ray fluorescence spectrometer was utilized for generating elemental data. Each sample was analyzed on cleaned, diamond-blade cut surfaces under helium purging to enhance light element sensitivity (specifically Al, Mg, P, Si) and to prevent heavy element masking. Samples were measured in total for a 780-s count time under three analytical filters for the detection of different groups of elements: [1] main-range filter ($Z = 21–80$) for a 240-s count time, [2] low-range filter ($Z = 19–24$) for a 240-s count time, and [3] light-range filter ($Z \leq 17$) for a 300-s count time. Elements lighter than Na are not measurable. Measurements of known elemental values from international standards (Marine Sediment, MAG-1, Cody Shale, SCo-1, Green River Shale, SGR-1) and internal reference materials of similar genetic make-up were used to calibrate the elemental data. Calibration factors were calculated by using the method described in Martin and Carr (2020).

All 145 MRB samples were analyzed in the William Smith Laboratories of Geography, Geology and the Environment (GGE) at Keele University (U.K.). Plotting of the elemental data and statistical analysis were performed using the scientific data analysis software Past 3.x (Hammer et al., 2001).

3.2.3. Data control/cluster analysis

It is common practice with modern instruments such as XRF to produce vast quantities of multivariate, high-quality data. With the ability to generate such large datasets it becomes essential to analyze, interpret, and present them accurately. Here we subject the calibrated XRF dataset to agglomerative Hierarchical Cluster Analysis (HCA) to generate genetically similar data clusters between elemental variables that can be used to define the chemofacies for the 145 MRB samples. HCA is a multivariate statistical approach to sort data plotted in a hyperdimensional space based on the degree of similarity between the individual datum and its neighboring clusters (Turner, 2016). Clusters have been generated using Ward Jr's (1963) method of minimum variance and Euclidean distance (the direct distance between two centroids). This along with Principal Component Analysis (PCA) are typically the most widely used statistical approach for subdividing units in chemostratigraphic studies (Kirschvink, 1980; Güler et al., 2002; Montero-Serrano et al., 2010; Alassane et al., 2015; Heij et al., 2016; Turner et al., 2015; Turner et al., 2016; Rowe et al., 2017; Driskill et al., 2018). Organizing the calibrated XRF-dataset in this manner enabled the definition of sub-lithofacies-scale associations and provided a transparent basis for the comparison to MRB datasets published in the existing literature.

3.3. Geochemical classification of marine red beds

Currently a unified geochemical classification scheme for MRBs is lacking, although Neuhuber and Wagreich (2009) geochemical classification of CORBs has been successfully utilized for characterizing Paleocene MRBs from the Zagros Mountains (Khorassani et al., 2015). The geochemical classification of CORBs builds upon the lithological classification scheme introduced by Wagreich et al. (2009) and Wang et al. (2009). It is derived from Hay et al.'s (1984) classification of recent pelagic-hemipelagic sediments using [1] red pelagic clays, [2] calcareous ooze, and [3] siliceous ooze. The lithological classification scheme utilizes studied CORB successions from around Europe (Hu et al., 2005, 2006; Wagreich and Krenmayr, 2005) and distinguishes them into three lithological groups (and subsequent endmembers): [1] clayey CORBS, [2] calcareous CORBs and [3] siliceous CORBs (Fig. 1A). Neuhuber and Wagreich (2009) geochemical classification scheme is the result of a compilation of XRF-based inorganic geochemical data from various CORB profiles worldwide and uses these elemental data

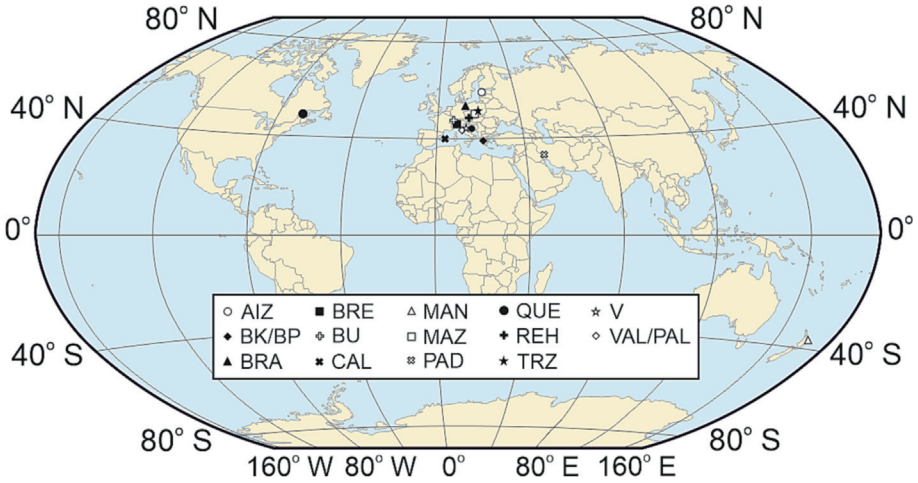

Fig. 4. Present-day global map showing the localities of the discussed marine red bed profiles: AIZ = Aizpute, BK = Karpenision, BP = Plaka, BRA = Brandenberg, BRE = Breggia Gorge, BU = Buchberg, CAL = Cala Mica, MAN = Manganotone, MAZ = Mazak, PAD = Padbeh, PAL = Pale Vallone, QUE = Quebec, REH = Rehkogel, TRZ = Trzemesnia, V = Vispi, VAL = Valdorbia. (For interpretation of the references to color in this figure legend, the reader is referred to the web version of this article.)

to define the three geochemical endmembers of Al-, Ca-, and Si-CORBs. This scheme was later adapted by Hu et al. (2012) based on the concentrations of Al_2O_3, CaO and SiO_2 and the mineralogical compositions extracted from a comprehensive dataset generated from 34 profiles (Hu et al., 2012, with references therein) (Fig. 1B).

The present study utilizes the geochemical classification scheme for CORBs by Neuhuber and Wagreich (2009) and Hu et al. (2012) to characterize Viséan MRBs from Menorca with regards to the three geochemical endmembers of Al-MRBs (clayey), Ca-MRBs (calcareous) and Si-MRBs (siliceous) by using Al_2O_3, CaO and SiO_2 concentrations. Furthermore, this study compiles XRF data of MRBs from different geological ages from the existing literature to compare and contrast the chemical element patterns of the HCA-generated chemofacies of the Viséan MRBs from Menorca. The compilation of geochemical studies of MRB profiles from the literature comprises of: Cambrian flysch facies from the Quebec Appalachian Province (Lajoie and Chagnon, 1973), MRB profiles from Telychian deep shelf facies from the East Baltics (Kiipli et al., 2000), CORB profiles from Italy (Hu et al., 2009), the Alps (Neuhuber et al., 2007; Neuhuber and Wagreich, 2009), New Zealand (Hikoroa et al., 2009), the Polish Flysch Carpathians (Bąk, 2007; Jiang et al., 2009), the Greek Pindos Mountains (Baltuck, 1982) as given in Neuhuber and Wagreich (2009) compilation, Pliensbachian and Toarcian Ammonitico Rosso facies in Italy and Switzerland (Hallam, 1967; Ortega-Huertas et al., 1993), Paleogene red and purple shales from the Zagros Mountains, Iran (Khorassani et al., 2015) and recent Pacific red clays (Bischoff et al., 1979; Glasby, 1991) (Fig. 4). Table 1 gives a summary of the dominant MRB lithofacies type and number of samples used for elemental analysis from each MRB profile.

4. Results

From the 145 MRB samples analyzed by XRF throughout the Cala Mica section, measurements of the concentrations of 9 major elements (Al, Ca, Fe, K, Mg, Mn, P, Si, Ti) and 10 minor elements (V, Cr, Cu, Zn, As, Rb, Sr, Zr, Mo, Pb) were gathered (see Tables S1 and S2, supplementary material). Major elements are expressed as oxide wt% with total iron (sum of divalent and trivalent iron) expressed as Fe_2O_3T and minor elements are given in ppm. Values of Al_2O_3 range between 1.64 and 30.48 wt% with an average of 20.55 wt%, CaO ranges between 0.28 and 38.74 wt% with an average of 7.66 wt%, SiO_2 ranges between 17.49 and 61.65 wt% with an average of 44.50 wt% and Fe_2O_3T values have an average of 7.15 wt% and a range between 2.04 and 14.25 wt% (see Table S1). The variation within the dataset indicates the breadth of geochemical heterogeneity throughout the Menorcan MRBs and the need to subdivide macroscopically homogenous appearing lithologies into different MRB types.

4.1. Lithofacies and marine red bed petrography

Ten lithofacies types were identified throughout the Cala Mica section (see Table 2), including three distinctive MRB facies [1] of red

Table 1
Summary of the profiles used for marine red bed geochemical studies. n = number of samples.

Code	Place	Section	Age	Author (s)	Lithofacies	n
AIZ	Latvia	Aizpute	Telychian	Kiipli et al., 2000	Red claystone	6
BK	Greece	Karpenision	Santonian	Baltuck, 1982	Red marls	2
BP	Greece	Plaka	Santonian	Baltuck, 1982	Red marls	4
BRA	Austria	Brandenberg	Cenomanian- Turonian	Neuhuber and Wagreich, 2009	Red limestone	4
BRE	Switzerland	Breggia Gorge	Pliensbachian- Toarcian	Hallam, 1967	Red marls	2
BU	Austria	Buchberg	Turonian	Neuhuber et al., 2007	Red marl and limestone	7
CAL	Spain	Cala Mica	Viséan	This study	Red mudstone	145
MAN	New Zealand	Manganotone	Turonian	Hikoroa et al., 2009	Red mudstone	7
MAZ	Poland	Mazak	Cenomanian	Jiang et al., 2009	Red and gray pelagic mudstone	16
PAD	Iran	Pabdeh	Late Paleogene- Early Eocene	Khorassani et al., 2015	Red and purple shales	10
PAL	Italy	Pale Vallone	Toarcian	Ortega-Huertas et al., 1993	Red nodular marls	2
QUE	Canada	Quebec	Cambrian	Lajoie and Chagnon, 1973	Red claystone	50
REH	Austria	Rehkogel	Santonian	Neuhuber and Wagreich, 2009	Red marl and limestone	4
TRZ	Poland	Trzemesnia	Turonian	Bąk, 2007	Red shale and mudstone	13
V	Italy	Vispi	Turonian	Hu et al., 2009	Scaglia rossa limestones	20
VAL	Italy	Valdorbia	Toarcian	Ortega-Huertas et al., 1993	Red nodular marls	3

Table 2
Main characteristics and interpretation of lithofacies from the Cala Mica section of Menorca (Spain).

Lithofacies	Code	Characteristics	Interpretation
Radiolarian chert	Rc	Dark to light gray with pale green hues, well bedded predominantly homogenous biogenic siliceous chert, typically between 0.5 and 5 cm thick, bed thickness divided by black siliceous mudstone horizons. Radiolarian tests show prominent dissolution features and recrystallization; weathered surface is highly fractured and oxidized.	Deposition of radiolarian tests with a periodic extremely distal detrital material influx in an ultra-deep marine, basinal environment under very low energy conditions with low sediment accumulation rates, below the CCD.
Green mudstone	Gm	Pale green and light gray calcareous planar-laminated mudstone, typically between 1 and 4 cm bed thickness with recrystallized calcitic horizons and finely dispersed pyrite, also recrystallized upon brownish bedding planes. Dendritic and mottled weathered surface.	Suspension deposition of minor detrital influx during periods of relatively reducing/stagnating conditions within a very low energy, distal deep-marine environment, above the CCD.
Brown and dark-gray, fine-grained sandstone and siltstone	Bss	Brown, fine-grained planar-laminated micaceous sandstone, 0.5 cm thick, intercalated with dark-gray siliceous siltstone that very slightly fines upward over 20 cm into lighter gray calcareous mudstone. Pale green colored laminations 0.1 to 0.2 cm in thickness, transition into orange, then burgundy upwards, evidence of poorly preserved bioturbation at the top of the unit. Dissolved radiolarian tests and mica grains infilled with recrystallized calcite.	Period of increased clastic input into a deep-marine, basinal environment, transition from relatively reducing to oxidizing conditions.
Red mudstone	Rmu	Reddish brown to burgundy, planar-laminated homogenous mudstone, sometimes with darkened cylindrical burrows 0.5 to 1 cm across and *Zoophycus*. Occasionally with moderately well preserved crinoidal stems.	Suspension deposition of minor detrital influx during periods of moderately oxidizing conditions, within a very low energy and distal environment.
Red pelagic limestone	Rpl	Fossiliferous reddish brown to dark gray clayey pelagic limestone comprised of a calcareous clayey matrix and predominantly fragmented crinoidal bioclasts. Typically, between 2 and 6 cm thick, varying laterally, with bioclasts depicting a fining upwards trend.	Mixed deposition of terrigenous and bioclastic material, during periods of elevated bioproductivity under oxidizing conditions within a distal environment, above the CCD.
Red silty mudstone	Rsm	Reddish brown to burgundy planar-laminated silty mudstone, poorly defined beds typically 0.5 to 2 cm thick. Bioturbation regularly throughout, occasionally with moderately well preserved crinoidal stems and small recrystallized brachiopods.	Deposition of detrital influx during periods of enhanced bioproductivity, under relatively oxidizing conditions, within a low energy and distal marine environment.
Yellow siltstone	Ys	Brownish yellow to yellow, planar bedded micaceous gritty siltstone, beds are typically 2 to 5 cm thick, intercalated with Rsm. Gritty organic-rich black horizons define bedding planes, occasional crinoid stems present.	Deposition of increased detrital influx under relatively reducing conditions, within a low energy and distal marine environment.
Thinly bedded limestone	Ltb	Light gray to yellowish gray thinly bedded, clast-supported microbreccias. Beds are typically between 1 and 4 cm thick and are found overlying Ls facies; clasts are predominantly poorly preserved crinoid stem fragments. Matrix comprised of yellowish gray lime-mud.	Deposition of re-worked carbonate material from underlying Ls facies during periods of increased environmental energy from low-density turbidity currents.
Light gray brecciated limestone	Lbr	Light gray clast-supported limestone breccia comprised of large (up to 30 cm long) sub-rounded micritic sheet-like planar clasts of Ls facies, sub-planar orientated parallel to bedding surfaces within a yellowish calcareous muddy matrix. Dewatering structures into mud beneath, erosive surface.	Deposition of re-worked carbonate material during high energy, non-newtonian flow conditions as a result of high-density turbidity currents into the deeper marine realm. Debris flow/?tempestite deposit.
Light gray limestone	Ls	Light gray to brownish colored lenticular bedded micritic limestone, beds typically thicken upwards from 1 to 3 cm to >4 cm and are regularly discontinuous and broken up. Occasional poorly preserved, recrystallized crinoid stems, beds depict dewatering structures with underlying Rmu facies.	Deposition of lithified or partially lithified carbonate material during periods of increased environmental energy.

mudstone (Rmu), [2] red pelagic limestone (Rpl) and [3] red silty mudstone (Rsm) which are discussed in detail below. The bedding, grain size, biogenic content and sedimentary structure characteristics of the different lithofacies indicate deposition within a low energy, deep-marine, basinal environment near to the CCD that was subjected to debris flow events depositing re-worked carbonate material from a distant carbonate shelf. The succession depicts an overall shallowing upward trend characterized by alternations of marine red beds and gray limestones, of which the MRBs display progressively more proximal features upward stratigraphy. The base depicts a transition from radiolarite deposition into MRBs of Rmu and Rpl facies (Fig. 5A), which could be associated with a change in redox conditions and/or increase in sediment supply related to eustatic sea-level change. This transitional succession is approximately 50 cm in thickness and capped by a sharp, erosive contact with the overlying Ls facies, which continues with re-worked clast-supported limestone conglomerates of Lbr facies overlain by finely re-worked, less chaotic limestones of the Ltb facies. This association suggests evidence of waning flows following either storm-like events or (? storm-induced) turbiditic events, which led to the deposition of the carbonate material. It is difficult to distinguish in this facies association between tempestites and turbidites as below storm wave base distal tempestites are known to exhibit turbidite-like character (Myrow, 2005). Four more cycles of MRBs and gray limestones occur over 3 m, with Rmu dominating most of the succession and Rpl becoming more fossiliferous and redder with the appearance of crinoidal horizons no >5 cm thick (Fig. 5B). Further evidence for distal tempestite/turbidites is seen in the sharp and erosive contacts of Ls facies with the underlying Rmu facies, where regular and prominent load cast structures are present, often separated from the main body of the limestones as clasts within the Rmu facies (Fig. 5C). Following this, the succession is dominated by cycles of red silty mudstones (Rsm) and yellow siltstones (Ys) that sometimes contain organic-rich pyritic horizons for 1.5 m; each cycle is typically between 10 and 30 cm in thickness (Fig. 5D). The succession is finally capped off by Quaternary dune deposits.

4.1.1. Red mudstone (Rmu)

The planar-laminated argillaceous red mudstone facies (Rmu) is the first and most frequently appearing MRB lithofacies throughout the Cala Mica section. It comprises of 0.5 to 1 m thick units often intercalated with red pelagic limestone (Rpl) facies and occasional crinoidal debris horizons. The weathered surface is brownish colored. The color changes slightly from the base of the succession starting as dark burgundy,

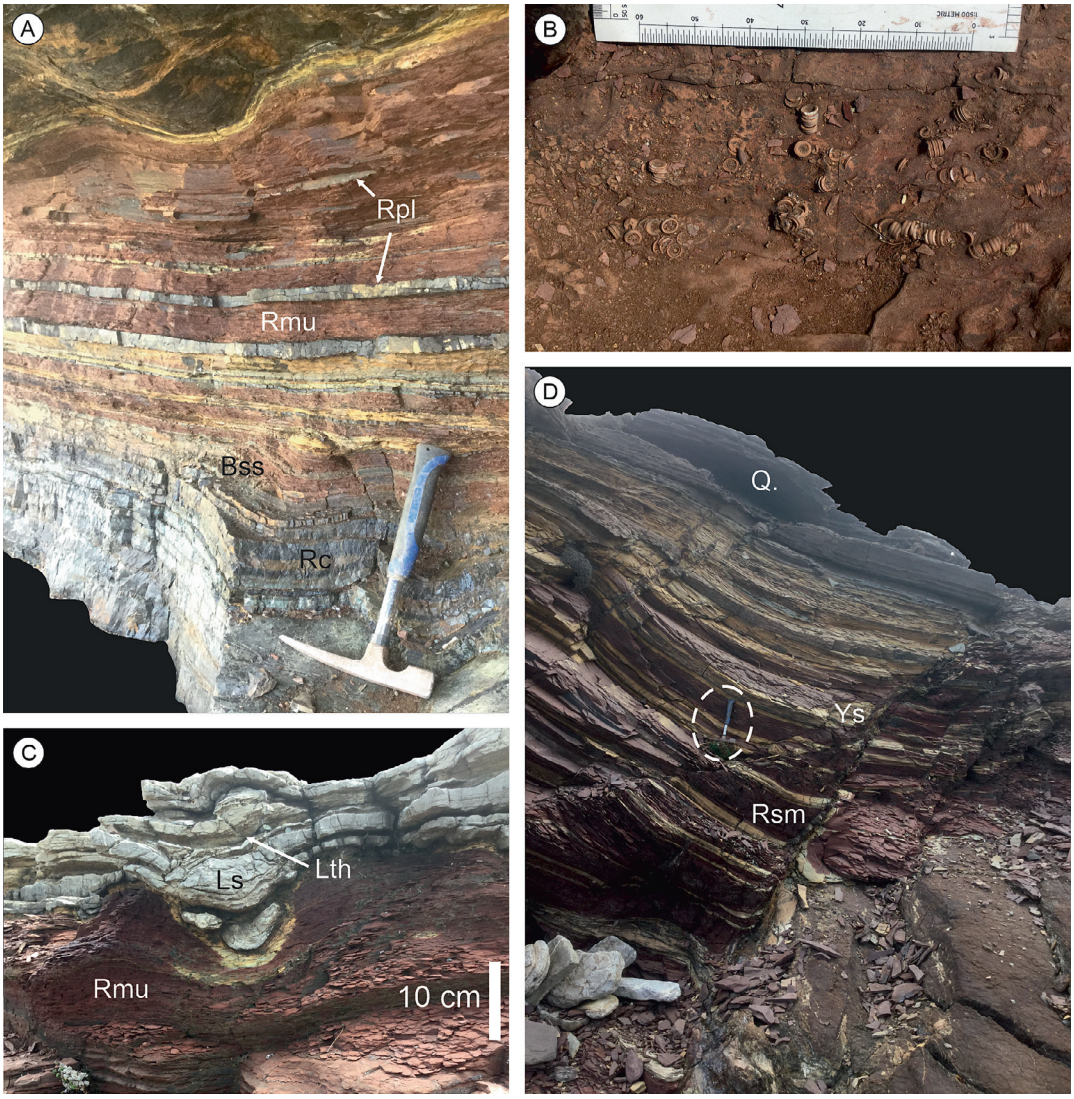

Fig. 5. Field photographs depicting the facies observed in the Cala Mica section of Menorca (Spain): (A) transition from dominantly radiolarian chert deposition to marine red bed facies at the base of the succession, size of hammer for scale is 28.5 cm. (B) partially disarticulated stems of *Balearocrinus breimeri* within facies Rpl towards the top of the succession. (C) load cast soft sediment deformation caused by limestone facies Ls sinking into marine red bed facies Rmu; localized chemical reduction occurs around the contact. (D) interbedded Rsm facies and Ys facies towards the top of the succession, capped by Quaternary sands (Q), size of hammer for scale is 28.5 cm. (For interpretation of the references to color in this figure legend, the reader is referred to the web version of this article.)

becoming redder up section with an increased presence of bioturbation within the top 1 m. In thin section Rmu depicts a pelleted siliceous mudstone planar feature and is mainly comprised of clay minerals with finely dispersed diagenetic mica and pyrite as well as rounded to sub-angular quartz grains up to 100 μm in size (Fig. 6A). Prominent staining from organic and iron-rich phases is dispersed homogenously throughout Rmu, displaying an array of geometries such as sub-angular (possibly detrital) hematite grains up to 10 μm across and concentric, circular structures up to 5 μm across that sometimes form clusters, possibly remnants of iron coccoids (Fig. 6B).

4.1.2. Red pelagic limestone (Rpl)

The crinoid-bearing red/reddish brown to burgundy pelagic limestone facies (Rpl) occurs in small beds up to 6 cm thick within the Rmu facies, with a mottled dark gray to reddish brown weathered surface (Fig. 5A). The bed geometry of Rpl shows some variation throughout the Cala Mica section, with slightly lenticular beds that tend to be more argillaceous and grayer accompanied with highly lenticular, fining upward beds that yield greater assemblages of partially disarticulated crinoids which are typically redder (Fig. 5B). In thin section Rpl depicts a red colored iron-rich granular to microcrystalline calcareous clay cement with biogenic micrite crusts and re-worked bioclastic debris of varying size, mostly between 30 and 150 μm (Fig. 6C). The bioclasts appear to mostly be crinoidal fragments with foraminifera depicting relict agglutinated structures, brachiopod shells and possible trilobite pleura, all of which show evidence of dissolution (Fig. 6D).

4.1.3. Red silty mudstone (Rsm)

The red/pinkish brown to burgundy silty mudstone facies (Rsm) occurs within the top 1.5 m of the Cala Mica section and has a brownish burgundy to light gray weathered surface (Fig. 5D). Rsm is prominently intercalated with yellow, organically enriched siltstones (Ys facies), occurring in planar-laminated units between 0.2 and 0.5 m in thickness with black silty horizons. Rsm displays the highest degree of bioturbation out of the three MRB lithofacies with back-fill and burrowing structures present as well as containing small, poorly preserved brachiopods.

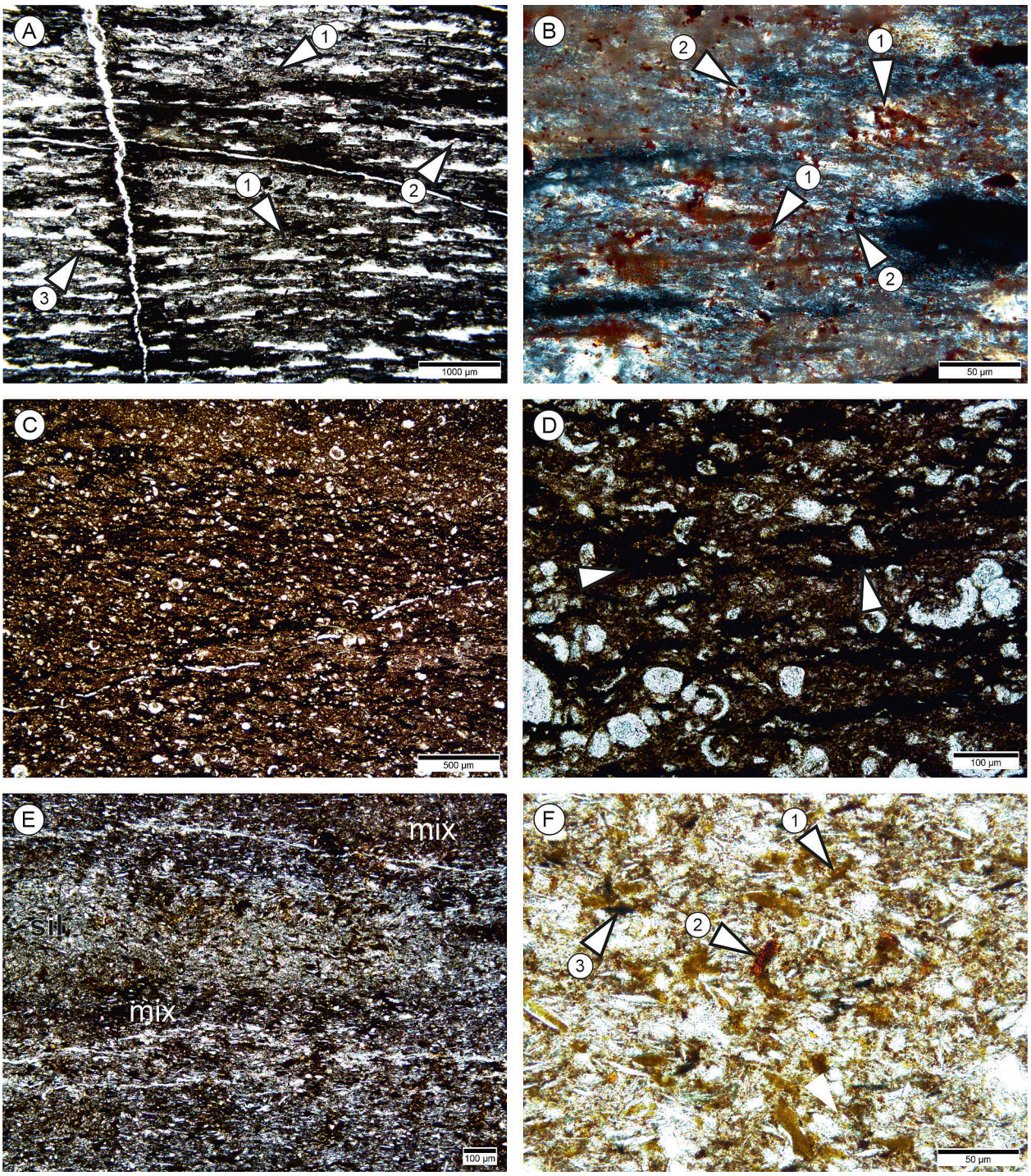

Fig. 6. Photomicrographs of Viséan marine red bed facies from the Cala Mica section of Menorca (Spain); (A) Red mudstone (Rmu) facies (sample CalB-46) of siliceous discontinuous/disrupted recrystallized laminae forming a pelleted planar feature with a high clay mineral content (white triangle 1). Rounded to sub-rounded quartz grains (white triangle 2) and radiolarian tests can be distinguished (white triangle 3) on top of the laminae. (B) Red mudstone (Rmu) facies (sample CalB-46) depicting a finely dispersed red colored iron-rich phase (hematite) residing in a range of geometries such as concentric circular structures typically <5 µm, sometimes forming aggregates/clusters (iron coccoids?) (White triangle 1) and sub-angular grains approximately 5 µm across (white triangle 2). (C) Red pelagic limestone (Rpl) facies (sample CalA-12) of fine-grained red stained marl with a granular to microcrystalline calcareous clay cement containing re-worked calcitic bioclasts with a size between 20 and 150 µm. (D) Red pelagic limestone (Rpl) facies (sample CalA-12) displaying an organic-rich micritic (?) envelope network (white triangles) between recrystallized calcite bioclast allochems. (E) Red silty mudstone (Rsm) facies (sample CalA-30) depicting yellow to orange, brown silt laminae (sil) and mixed reddish-brown silt and mud laminae (mix). (F) Red silt-mudstone (Rsm) facies (sample CalA-30), silt laminae depicting three different colors of yellowish (goethite?) (white triangle 1), red (hematite) (white triangle 2) and reddish dark brown (organic-rich?) (gray triangle). (For interpretation of the references to color in this figure legend, the reader is referred to the web version of this article.)

Rsm has a grittier texture than the underlying Rmu facies, it contains a reduced clay-bearing phase and a greater detrital component which is comprised of sub-angular to sub-rounded quartz grains that are typically 10 to 50 µm across and muscovite flakes that are typically 20 to 40 µm across (Fig. 6E). This facies contains more dispersed organic material and a higher content of an iron-phase. Within the matrix, globular structures are present albeit not as well preserved as in the Rmu facies (Fig. 6D).

4.2. Menorcan MRB geochemistry

Geostatistical analysis of the XRF elemental data from the 145 MRB samples collected from the Cala Mica section yielded 13 high-resolution chemofacies. To generate the chemofacies 14 normalized major and minor elemental variables (Mg, Al, Si, P, K, Ca, Ti, V, Cr, Mn, Fe, Sr, Zr, Mo) from the analyzed samples were used to produce a dendrogram based upon the key driving elemental signatures (Fig. 7). The Phenon line in this study has been selected above the junction where the distance between clusters exceeds a value of 10 % of the maximum distance value (cf. Güler et al., 2002). The Menorcan MRBs discriminate predominantly as Al-MRBs. The defining geochemical characteristics of each chemofacies are therefore expressed as relative enrichment factors ($EF_{element}$) compared to Wedepohl's (1971) average shale in Fig. 8, with the enrichment factor data being presented in Table 3. Enrichment factors have been calculated using: $EF_{element} = (element/Al)_{sample}/(element/Al)_{average\ shale}$. In this study we define the elemental concentration within each chemofacies being enriched when $EF_{element} \geq 5$ and depleted when $EF_{element} \leq 5$ following the method used by Turgeon and Brumsack (2006) and as utilized in analyzing CORB samples by Hu et al. (2012). Aluminum, which is typically immobile during diagenesis (Calvert and Pedersen, 1993), is considered here to reside within the aluminosilicate minerals and is used as an indicator for the terrigenous influx of detrital material from the hinterland. The major and minor elemental data for the MRB samples have been normalized against Al_2O_3 to determine the overall geochemical character of the established chemofacies and what geochemical systems are at play with respect to the terrigenous fraction (see Figs. 9 and 10). For reference and comparison all data are plotted together with Turekian and Wedepohl's (1961) average composition of [1] shale, [2] carbonate, [3] deep-sea carbonate and [4] deep-sea clay as well as Wedepohl's (1995) average composition of the [5] upper continental crust.

4.2.1. Major elements

Major elements within Menorcan MRBs are generally depleted relative to Wedepohl's (1971) average shale except for MgO, CaO and MnO (Fig. 8A). K_2O, TiO_2 and Fe_2O_3T values are similar to Wedepohl's (1971) average shale, although can be considered slightly depleted, with the exception of Fe_2O_3T values for chemofacies C1, C5 and C13 that are not depleted (EF_{Fe} = 2.29, 1.27 and 1.25, respectively). MgO is enriched in chemofacies C1 (EF_{Mg} = 18.48) and slightly enriched in chemofacies C5 and C12 (EF_{Mg} = 3.04 and 1.64, respectively) (Fig. 8A). Chemofacies C7 is depleted in SiO_2 (EF_{Si} = 0.51), and the remaining chemofacies are generally depleted compared to Wedepohl's (1971) average shale except C1 (EF_{Si} = 2.73). This is similar for the values of P_2O_5 where C5 and C12 are depleted (EF_P = 0.44 and 0.50, respectively), with the remaining chemofacies being depleted except C4 (EF_P = 1.06) suggesting an overall low bioproductivity. CaO is enriched in chemofacies C1, C2, C3, C4 and C5 and depleted in chemofacies C7, C10, C11 and C13 compared to Wedepohl's (1971) average shale. MnO values are consistently enriched throughout the succession, except for C7 and C8 (EF_{Mn} = 2.3 and 3.56, respectively) that are slightly enriched, indicating the presence of an external MnO source outside the sedimentary system, probably hydrothermal activity (Fig. 8A).

Values of MgO give two broad trends that poorly and negatively correlate with Al_2O_3, showing no evidence of affiliation within the terrigenous fraction (Fig. 9A). The negative trend correlates more so with deep-sea clay whereas there is no correlation with the average shale and upper continental crust of Turekian and Wedepohl (1961) and Wedepohl (1995). All MgO values are enriched relative to the deep-sea carbonate and are generally depleted compared with the average carbonate, except for chemofacies C1 (Fig. 9B). All SiO_2 values in Menorcan MRBs reach above average shale, carbonate, and deep-sea carbonate, and fall below upper continental crust. Two trends are visible which both show a positive correlation with Al_2O_3. The less positively correlating trend is seen to plot more closely to deep-sea clay, suggesting a more pelagic setting with respect to the remainder of the dataset. P_2O_5 forms a weak positive correlation with Al_2O_3 and is on average depleted relative to all used international standards which could suggest a low bioproductivity at the time of deposition (Fig. 9C). Values of K_2O strongly positively correlate with Al_2O_3 (R^2 = 0.96), indicating K_2O is residing fully within the terrigenous fraction and a lack of diagenetic remobilization (Fig. 9D). CaO is depleted relative to the average carbonate and the deep-sea carbonate and forms two negative trends with Al_2O_3, indicating that CaO is residing within the carbonate fraction (Fig. 9E). TiO_2 (Fig. 9F) correlates strong positively with Al_2O_3 (R^2 = 0.82), indicating that it is residing within the terrigenous fraction. It is generally depleted relative to the average shale, the deep-sea clay, and the upper continental crust. MnO forms two broad trends that negatively correlate with Al_2O_3.The two trends intersect at approximately 20 wt% Al_2O_3 and 1.5 wt% MnO (Fig. 9G). The concentrations of MnO are enriched relative to all used international standards, except for deep-sea clay that plots closer to the less negative trend. Fe_2O_3T correlates positively with Al_2O_3. It is enriched relative to the average carbonate and deep-sea carbonate, and depleted against the deep-sea clay, whilst showing more affinities with the average shale and the upper continental crust (Fig. 9H) (Turekian and Wedepohl, 1961; Wedepohl, 1995). The Menorcan MRBs can be classified as Al-MRBs, with the exception of chemofacies C1, C3, and C4 that class as Ca-MRBs (Fig. 9I).

Concentrations of P_2O_5, K_2O, TiO_2 and Fe_2O_3T show a positive correlation with Al_2O_3 indicating a genetic relationship between these oxides and Al_2O_3. Values for K_2O and TiO_2 show a strong positive correlation against Al_2O_3 (R^2 = 0.96 and 0.82, respectively) indicating that both are residing within the terrigenous fraction in clay and heavy mineral phases, respectively such as illite and rutile. Values for P_2O_5 and Fe_2O_3T exhibit a weaker positive correlation with Al_2O_3 (R^2 = 0.53 and 0.51, respectively) indicating their presence within the terrigenous fraction but also in other fractions present in the sedimentary system such as authigenic and secondary diagenetic minerals like apatite and hematite, respectively.

Concentrations of SiO_2 correlate positively with Al_2O_3 and are forming two trends: A SiO_2 depleted and a SiO_2 enriched trend. The SiO_2 depleted trend is formed by chemofacies C2, C3, C4, C6, C7, C8, C9 whereas the SiO_2 enriched trend is constituted by chemofacies C5, C10, C11, C12. Chemofacies C13 is plotting intermediate between the two trends and C1 is plotting close to average deep-sea carbonate and carbonate. The first trend strongly correlates with an R^2 = 0.92, indicating the SiO_2 concentration within these chemofacies is residing purely within the terrigenous fraction as quartz, the second trend correlates with an R^2 = 0.65 suggesting a dilution by CaO. The high Si/Al and Si/Ti ratios are indicative for excess silica (Marsh et al., 2007; Agnihotri et al., 2008; Dickson et al., 2010). For the Menorcan MRBs this excess silica is interpreted to be derived from the accumulation of radiolarian tests.

Concentrations of CaO also form two distinct trends that correlate strong negatively with Al_2O_3. The two trends are formed by the same chemofacies groups as the two trends within the SiO_2/Al_2O_3-system (C2, C3, C4, C6, C7, C8, C9 and C5, C10, C11, C12). Both trends show high correlation coefficients (R^2 = 0.94 and 0.86, respectively). The first trend (R^2 = 0.94) exhibits affinities to the average carbonate and deep-sea carbonate standard whereas the second trend (R^2 = 0.86) shows a closer relation to the average shale, the deep-sea clay and the upper continental crust. The two trends are interpreted to highlight the effects of biogenic carbonate (excess carbonate) and biogenic silica (excess silica) sources outside the terrigenous fraction. The first trend is suggesting a biogenic elemental signal from calcium carbonate whereas the second trend shows a mixed biogenic elemental signal from calcium carbonate and silica. The concentration of biogenic carbonate can be distinguished from the terrigenous clay fraction by using Ca/Fe ratios (Hebbeln et al., 2006; Nizou et al., 2010), whereby

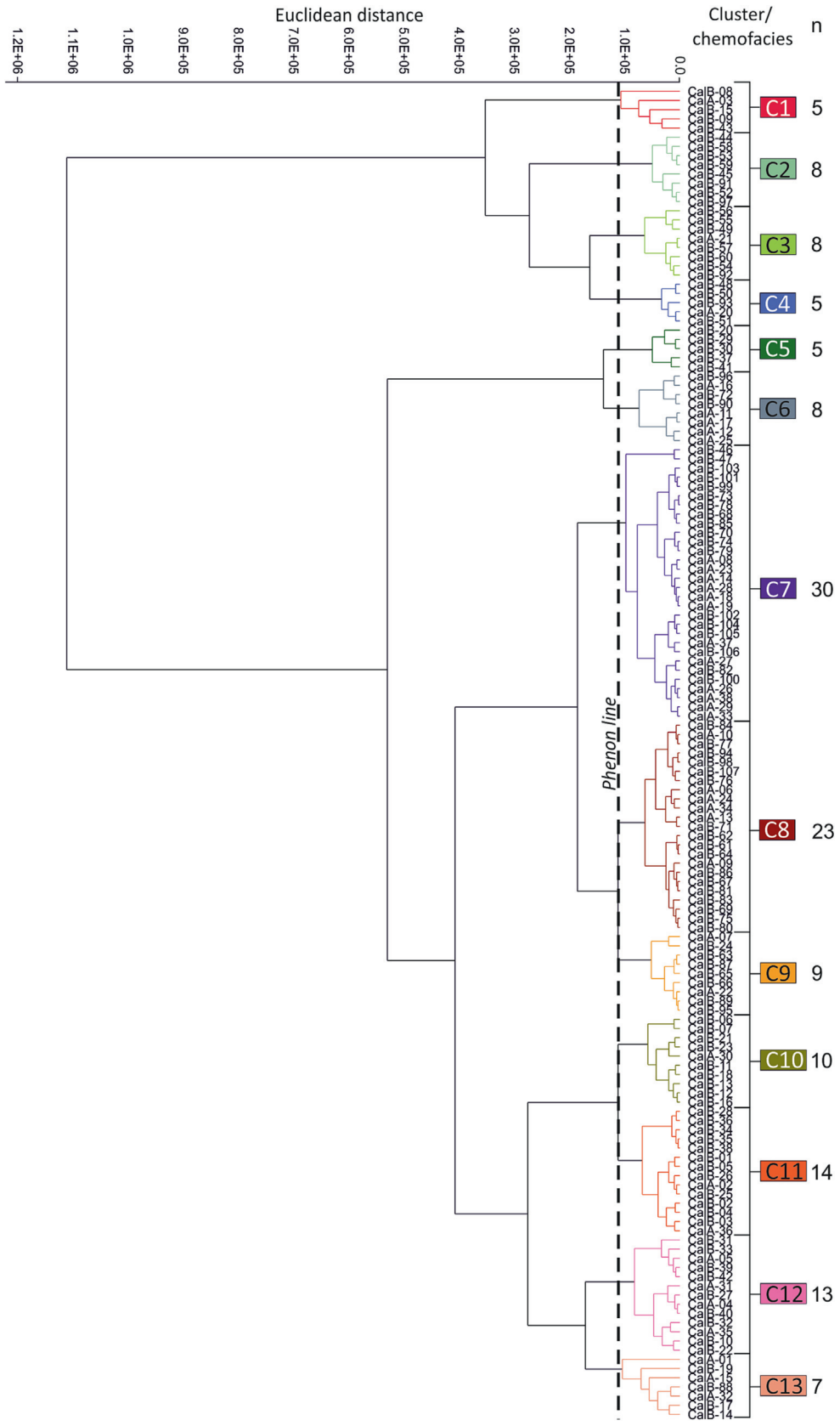

Fig. 7. Dendrogram illustrating the subdivision of the XRF-derived geochemical dataset (145 samples) into 13 chemofacies using Ward Jr's (1963) Hierarchical Clustering Analysis method (HCA). The width of a cluster on the x-axis represents the number of data points within that cluster; clusters are defined by the Phenon line which has been set at a value of 10 % of the maximum distance value (Güler et al., 2002; Turner et al., 2015). A total of 14 normalized variables have been used to form the clusters (Mg, Al, Si, P, K, Ca, Ti, V, Cr, Mn, Fe, Sr, Zr, Mo). (For interpretation of the references to color in this figure legend, the reader is referred to the web version of this article.)

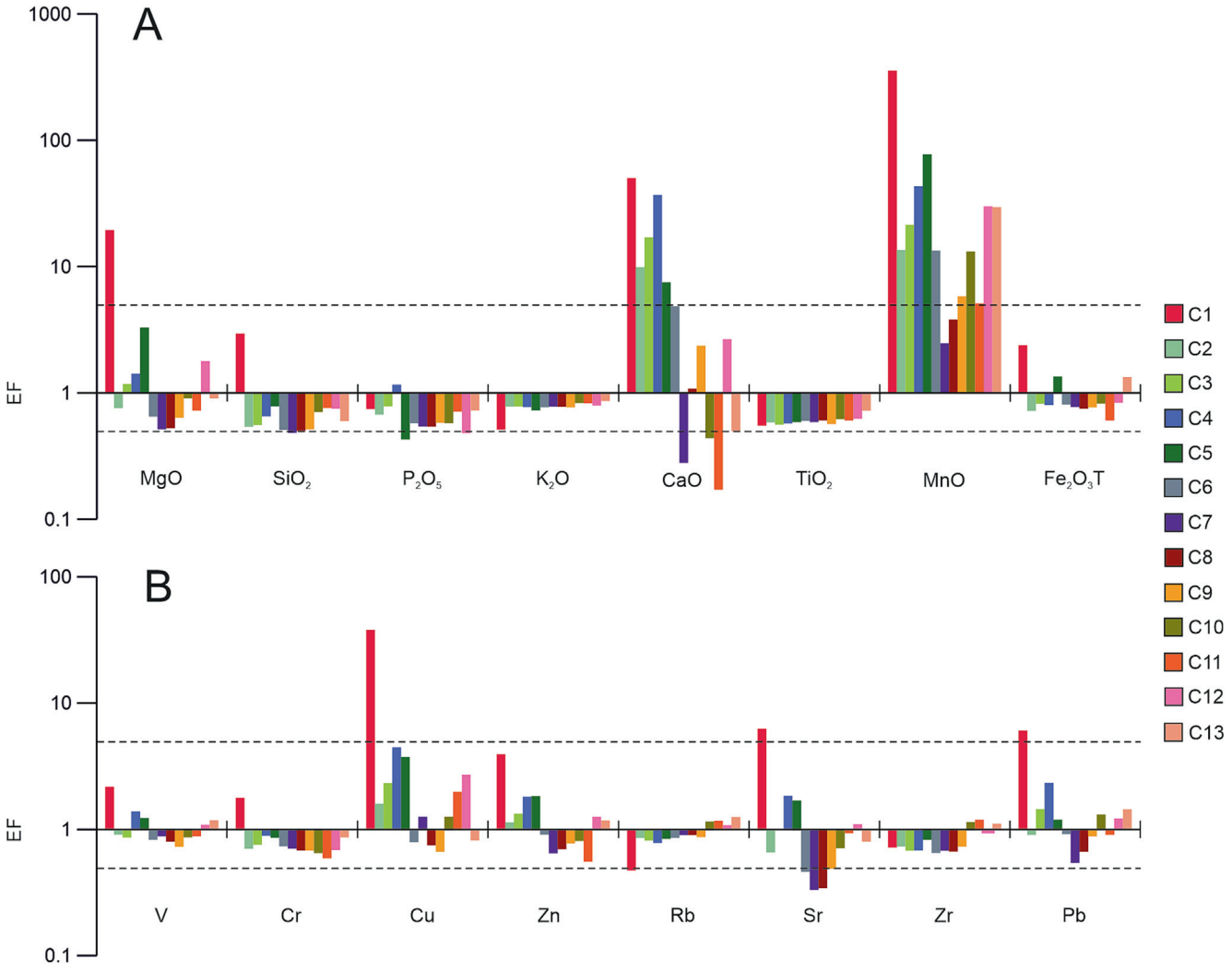

Fig. 8. Enrichment factors of hierarchical cluster analysis-generated chemofacies from Viséan marine red beds recovered from the Cala Mica section of Menorca (Spain), based upon comparison to Wedepohl's (1971) average shale elemental values. (A) Major elements. (B) Minor elements. (For interpretation of the references to color in this figure legend, the reader is referred to the web version of this article.)

chemofacies C2, C3, C4, C6, and C9 of the first trend have a higher average Ca/Fe ratio of 3.28 than chemofacies C1, C5, and C12 of the second trend which shows an average Ca/Fe ratio of 1.82, indicating an elevated biogenic carbonate contribution relative to the terrigenous influx. The remaining chemofacies (C7, C8, C10, C11 and C13) have very low CaO concentrations (1.64 wt% average) with an average Ca/Fe ratio of 0.2, indicating a very minimal influence from any biogenic sources.

The concentrations of MgO and MnO show a similar relationship to Al_2O_3. A negative correlating trend comprised of chemofacies C5, C10, C11, C12, and C13 ($R^2 = 0.50$ for MgO and 0.72 for MnO) except for

Table 3
Calculated enrichment factors compared to Wedepohl's (1971) average shale for the different chemofacies generated from Viséan marine red beds from the Cala Mica section of Menorca (Spain).

Chemofacies	MgO	SiO_2	P_2O_5	K_2O	CaO	TiO_2	MnO	Fe_2O_3T	V	Cr	Cu	Zn	Rb	Sr	Zr	Pb
C1	18.48	2.73	0.79	0.54	48.16	0.57	342.31	2.29	2.04	1.66	36.49	3.73	0.50	5.92	0.75	5.81
C2	0.81	0.56	0.71	0.83	9.31	0.61	12.73	0.76	0.97	0.75	1.50	1.06	0.92	0.70	0.77	0.97
C3	1.07	0.58	0.84	0.83	16.12	0.58	20.20	0.87	0.93	0.81	2.19	1.24	0.87	1.00	0.71	1.36
C4	1.30	0.69	1.06	0.82	35.26	0.60	40.90	0.85	1.30	0.96	4.22	1.71	0.83	1.73	0.71	2.21
C5	3.04	0.84	0.44	0.77	7.03	0.61	73.62	1.27	1.15	0.92	3.53	1.72	0.90	1.59	0.88	1.11
C6	0.69	0.53	0.60	0.82	4.51	0.63	12.57	0.86	0.89	0.79	0.85	0.97	0.92	0.48	0.68	0.99
C7	0.54	0.51	0.57	0.83	0.29	0.61	2.30	0.82	0.95	0.75	1.18	0.69	0.97	0.34	0.71	0.56
C8	0.55	0.52	0.57	0.83	1.00	0.63	3.56	0.79	0.86	0.73	0.80	0.74	0.97	0.36	0.70	0.70
C9	0.67	0.54	0.61	0.82	2.18	0.59	5.47	0.81	0.78	0.72	0.71	0.83	0.93	0.51	0.77	0.95
C10	0.97	0.75	0.61	0.89	0.46	0.65	12.37	0.87	0.93	0.69	1.18	0.87	1.08	0.76	1.07	1.22
C11	0.77	0.81	0.76	0.89	0.18	0.63	4.80	0.63	0.95	0.62	1.86	0.58	1.09	1.00	1.12	0.98
C12	1.64	0.80	0.50	0.85	2.46	0.65	28.32	0.89	1.02	0.73	2.55	1.17	1.01	1.03	0.99	1.14
C13	0.97	0.63	0.77	0.93	0.53	0.76	27.94	1.25	1.10	0.90	0.87	1.10	1.17	0.86	1.04	1.35
Average	0.91	0.61	0.62	0.84	2.83	0.63	12.47	0.84	0.94	0.75	1.55	0.87	0.98	0.65	0.81	0.91

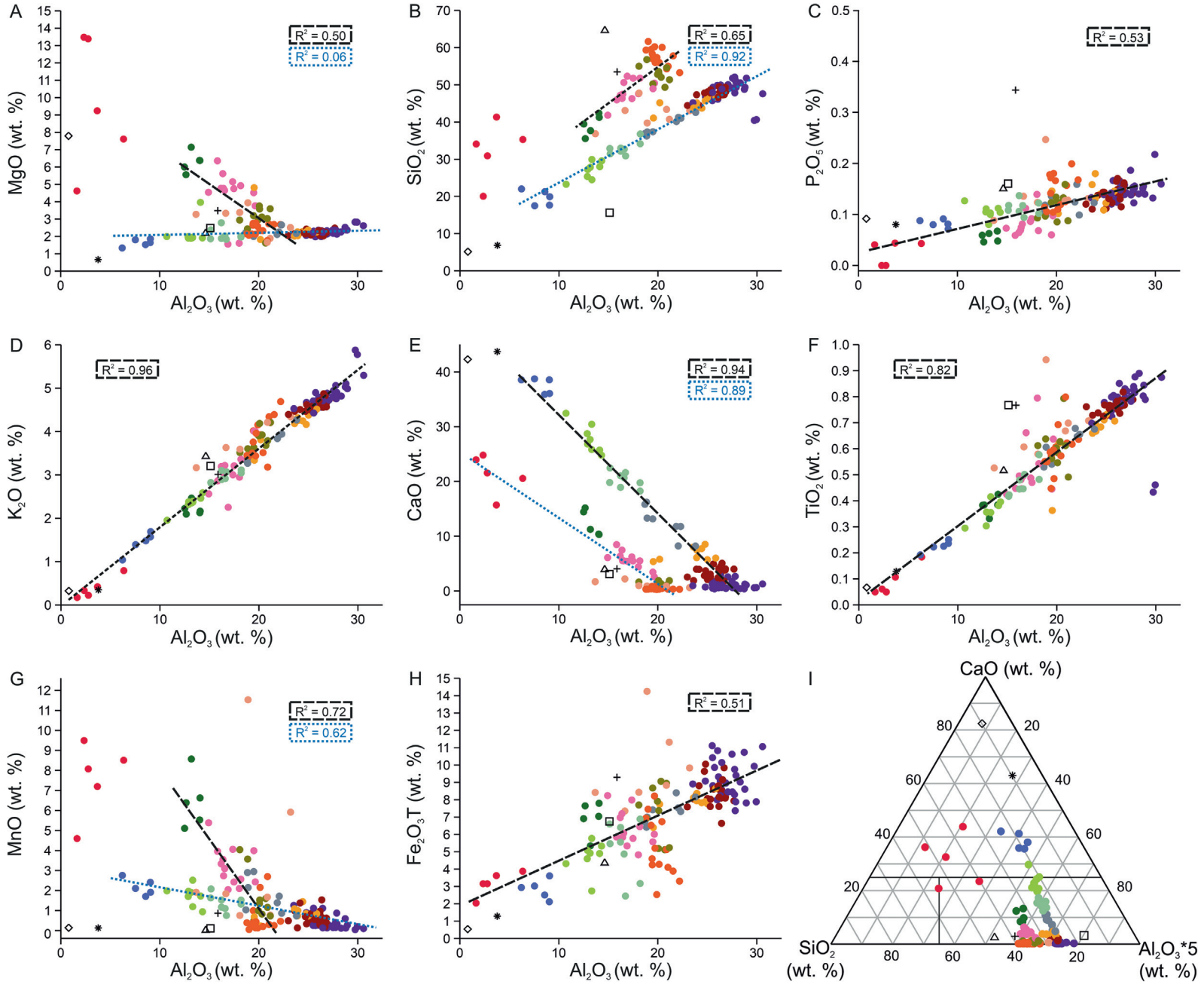

?0,0,0,0,0,1,0,0,0,0,5;0b7]Fig. 9. Major elements plotted against Al_2O_3 of Viséan marine red beds recovered from the Cala Mica section of Menorca (Spain): square = average shale, diamond = average carbonate, star = deep-sea carbonate, plus = deep-sea clay (Turekian and Wedepohl, 1961), triangle = average composition of upper continental crust (Wedepohl, 1995). (For interpretation of the references to color in this figure legend, the reader is referred to the web version of this article.)

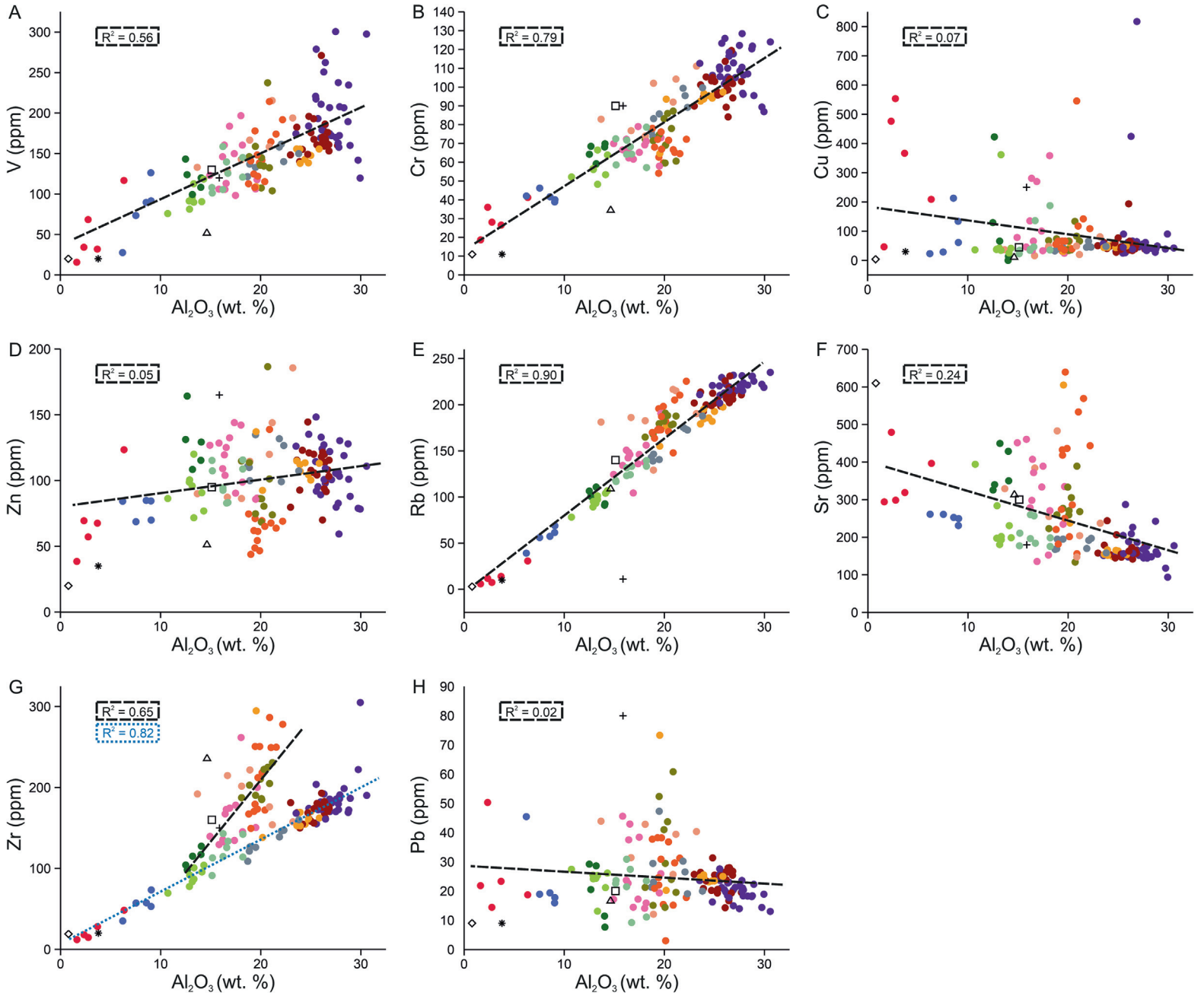

Fig. 10. Minor elements plotted against Al_2O_3 of Viséan marine red beds recovered from the Cala Mica section of Menorca (Spain): square = average shale, diamond = average carbonate, star = deep-sea carbonate, plus = deep-sea clay (Turekian and Wedepohl, 1961), triangle = average composition of upper continental crust (Wedepohl, 1995). (For interpretation of the references to color in this figure legend, the reader is referred to the web version of this article.)

chemofacies C1 that only weakly correlates for MgO. The second trend consisting of chemofacies C2, C3, C4, C6, C7, C8, and C9 also correlates negative for MnO ($R^2 = 0.62$) and exhibits no correlation for MgO ($R^2 = 0.06$). The more negative correlating first trend for MgO correlates well with CaO ($R^2 = 0.72$), indicating MgO is mainly residing within the carbonate fraction (potentially as dolomite). MgO for the second trend does not correlate well with any major oxides suggesting an external magnesium source is diluting and masking the signature of the sedimentary system. Values of MnO for both trends correlate positively with CaO ($R^2 = 0.51$ for the first trend and $R^2 = 0.58$ for the second), indicating the presence of similar quantities of manganese carbonate mineral phases such as e.g., rhodochrosite. MgO/MnO for the chemofacies C1, C5, C10, C11, C12, and C13 (which are forming the first trend) is correlating positive ($R^2 = 0.54$), whereas the second trend (C2, C3, C4, C6, C7, C8, and C9) produces no correlation. The MgO values show little variation compared to MnO, indicating that the Mn/Mg relationship is provided by different fractions.

4.2.2. Minor elements

Minor elements V, Cr, Cu, Zn, Rb, Zr and Pb are very similar to Wedepohl's (1971) average shale (Fig. 8B), with the Cr and Zr being generally slightly depleted and Cu being generally slightly enriched. Chemofacies C1 is consistently an exception. It exhibits enrichments in Cu, Sr, Zr and V, Cr, Zn, whilst being depleted in Rb (Fig. 8B). Chemofacies C5, C6, and C7 are depleted in Sr ($EF_{Sr} =$ 0.48, 0.34 and 0.36, respectively) suggesting a low contribution of biogenic carbonate. It has to be noted, that the single use of minor element proxies for paleo-productivity (P, Cu, Zn) and redox conditions (V, Cr) needs caution and that the interpretations with regards to paleobioproductivity and changes in the redox-regime are relative estimates and not absolute quantifications.

Concentrations of V correlate positively with Al_2O_3 but exhibit a larger scatter at elevated values. The V concentrations are similar to those of the average shale and deep-sea clay and enriched relative to the average carbonate, carbonate and upper continental crust (Fig. 10A). Cr correlates strong positive with Al_2O_3, is depleted relative to average shale and deep-sea clay, and enriched compared to the upper continental crust (Fig. 10B). Values of Cu do not show any particular correlation to Al_2O_3 and is similar in concentration to all used international standards apart from average deep-sea clay to which it is relatively depleted along with supposed outliers in the MRB dataset (Fig. 10C). Zn also does not show any correlation with Al_2O_3, producing a 'shotgun' spread of results. Zn values plot more closely with average shale and are depleted relative to deep-sea clay, whilst being enriched relative to average carbonate, deep-sea carbonate and upper continental crust (Fig. 10D). Rb correlates strong positively with Al_2O_3, indicating that Rb is residing solely within the terrigenous fraction (Fig. 10E). Sr shows a very weak negative correlation with Al_2O_3, although generally depicts no affinity to the terrigenous fraction. Its concentration is similar to average shale, deep-sea clay and upper continental crust, and depleted compared to the average carbonate (Fig. 10F). Zr shows two positive trends with Al_2O_3, the stronger positively correlating trend suggests Zr residing predominantly within the terrigenous fraction ($R^2 = 0.82$), whereas the relatively Zr-enriched trend indicates an additional source of Zr ($R^2 = 0.65$) (Fig. 10G). Average shale and deep-sea clay plot more closely to the relatively Zr-enriched trend. Pb values show no correlation with Al_2O_3 (Fig. 10H) and are depleted relative to deep-sea clay and enriched relative to average carbonate and deep-sea carbonate.

The redox sensitive elements V and Cr generally correlate positively with Al_2O_3 ($R^2 = 0.56$ and 0.79, respectively). Cr is depleted with respect to average shale and deep-sea clay implying mildly oxidizing conditions (Turekian and Wedepohl, 1961). The weaker correlation of V suggests its presence within the detrital and the authigenic fraction where V(III) substitutes for Al on the octahedral sites in authigenic clay minerals (Breit and Wanty, 1991; Tribovillard et al., 2006). Zr shows two positive linear trends with differing gradients of $R^2 = 0.82$ for chemofacies C1, C3, C4, C6, C7, C8, and C9 and $R^2 = 0.65$ for chemofacies C5, C2, C10, C11, C12, and C13. Zr is associated with heavy mineral phases such as zircon and is carried within the terrigenous fraction, whereby higher Zr values suggest elevated detrital influx from the hinterland and subsequently coarser sediment grain size when discriminated against other terrigenous elements such as Al, K, Rb and Ti (Calvert et al., 1996; Cuven et al., 2010; Kylander et al., 2011; Marshall et al., 2011; Wilhelm et al., 2013; Shala et al., 2014). Within the two positive Zr trends given by Menorcan MRB chemofacies, average shale and deep-sea clay plot with the lower Al_2O_3/Zr trend whilst average carbonate and deep-sea carbonate plot close to the higher Al_2O_3/Zr trend. The trends suggest two separate grain size pathways for the Menorcan MRBs that diverge at approximately 12 wt% Al_2O_3 and 100 ppm Zr, with the lower Al_2O_3/Zr trend indicating a change in the amount of terrigenous material entering the sedimentary system. The chemofacies that have a CaO concentration of >10 wt% (C1, C2, C3, C4, C5, and C6), generate a slightly negative trend of Sr with Al_2O_3 and a slightly positive correlation of Sr with CaO, indicating that Sr is most likely residing within the carbonate fraction of these chemofacies. The co-variation of Ca and Sr can be used to distinguish between detrital and biogenically derived Ca as Sr is utilized by calcifying organisms during Ca fixation. Therefore, Sr has also been used in the past as a proxy element for biological activity (Zaragosi et al., 2006; Richter et al., 2006). Chemofacies where SiO_2 concentrations tend to be higher (>50 wt%) exhibit a wider range and higher values of Sr than the chemofacies which are more Al_2O_3-rich, suggesting that they contain greater quantities of Sr that is probably residing within certain diagenetic mineral phases. Values of Pb plot similar to Sr with Al_2O_3 and CaO. The majority of Pb and Sr values plot within broad ranges apart from some seemingly enriched chemofacies-independent outliers that could have had an additional hydrothermal influence. This is also seen in the values of Cu that for the most part fall within a range between 0 and 150 ppm, except for enriched outliers that plot above average deep-sea clay, suggesting periodic hydrothermal interference. CaO-rich chemofacies such as C1 and C4 show a greater variation in Cu concentrations than the Al_2O_3-rich chemofacies, whereas the SiO_2-rich chemofacies exhibit greater variations in the Sr and Pb concentrations. Values of Zn do not show any distinct relationship with Al_2O_3, although Zn concentrations typically above 150 ppm in marine sediments have been associated with extremely high terrigenous supply (Hebbeln et al., 2006; Rothwell and Croudace, 2015). Aside from a few outliers, however, such elevated Zn concentrations are not present within the Menorcan MRBs.

4.3. Compilation of MRB geochemical data

The geochemical characteristics of MRBs from the literature (Table 1.) are discussed and compared with the 13 HCA-generated chemofacies from Viséan MRBs of the Cala Mica section, together with the total average of the 145 MRB samples recovered from the Cala Mica section. Table 4 gives the major element chemistry of the MRB profiles and average MRB geochemical endmember as well as the respective age of each dataset. For the Cambrian Quebec section and Telychian Aizpute section the geochemical Al-MRB endmember has been assigned based on their similar Fe_2O_{3T} contents that correlate more with other sections that have been classified as Al-MRBs as compared to Ca- and Si-MRBs. Values of Al_2O_3 range between 0.06 and 27.15 wt% with an average of 13.7 wt%, CaO ranges between 0.47 and 53. 09 wt% with an average of 16.84 wt% and SiO_2 ranges between 3.47 and 73.52 wt% with an average of 40.12 wt% (Table 4). Table 5 gives the minor element distribution; major elements are expressed in oxide wt% and minor elements are expressed in ppm.

4.3.1. Major elements

Values of MgO form two trends, a general positive correlation with Al_2O_3 which includes nearly all published MRB datasets and average

Table 4
Average major element chemistry for the different chemofacies from Viséan marine red beds recovered from the Cala Mica section of Menorca (Spain) and marine red bed profiles throughout the Phanerozoic (references found in Table 1) with standards; Wedepohl's (1971) average shale (a), Turekian and Wedepohl's (1961) average shale (b), average carbonate, deep-sea clay and deep-sea carbonate, and Wedepohl's (1995) average upper continental crust.

Section/ chemofacies	Age	Average MRB endmember	Al_2O_3		CaO		SiO_2		MgO		P_2O_5		K_2O		TiO_2		MnO		Fe_2O_3T	
			wt%	Stdev	wt%	Stdev	wt%	Stdev	wt%	Stdev	wt%	Stdev	wt%	Stdev	wt%	Stdev	wt%	Stdev	wt%	Stdev
Quebec	Cambrian	Al_2O_3 (?)	–	–	–	–	–	–	–	–	–	–	–	–	–	–	0.46	–	8.00	–
Aizpute	Telychian	Al_2O_3 (?)	–	–	–	–	–	–	–	–	–	–	–	–	–	–	–	–	8.97	1.25
C1	Visean	CaO	3.36	1.64	21.32	3.20	32.34	7.02	9.67	3.41	0.03	0.02	0.39	0.22	0.09	0.05	7.58	1.66	3.17	0.63
C2	Visean	Al_2O_3	16.57	1.10	20.32	1.31	33.01	1.71	2.09	0.31	0.11	0.01	2.97	0.12	0.47	0.05	1.39	0.37	5.17	1.51
C3	Visean	Al_2O_3	13.09	1.02	27.81	2.44	26.96	2.23	2.19	0.67	0.11	0.01	2.35	0.17	0.36	0.04	1.74	0.46	4.71	0.85
C4	Visean	CaO	8.09	1.09	37.56	1.29	19.66	1.84	1.63	0.19	0.08	0.01	1.44	0.22	0.23	0.02	2.18	0.37	2.84	0.50
C5	Visean	Al_2O_3	13.29	0.66	12.32	2.07	39.27	2.45	6.29	0.52	0.06	0.01	2.22	0.13	0.38	0.03	6.44	1.20	6.95	0.87
C6	Visean	Al_2O_3	20.75	1.85	12.32	2.82	39.11	2.24	2.22	0.18	0.12	0.02	3.67	0.34	0.61	0.06	1.72	0.82	7.37	0.63
C7	Visean	Al_2O_3	27.15	1.56	1.05	0.66	48.39	2.71	2.28	0.20	0.15	0.02	4.87	0.31	0.78	0.10	0.41	0.33	9.17	1.04
C8	Visean	Al_2O_3	25.67	1.16	3.39	0.95	47.47	1.52	2.20	0.12	0.14	0.02	4.59	0.14	0.76	0.03	0.60	0.36	8.39	0.76
C9	Visean	Al_2O_3	23.48	2.04	6.75	1.11	44.65	1.66	2.46	0.85	0.14	0.02	4.13	0.33	0.65	0.11	0.85	0.31	7.85	0.59
C10	Visean	Al_2O_3	19.96	0.94	1.22	0.51	52.89	2.25	3.02	0.63	0.12	0.02	3.83	0.24	0.61	0.08	1.63	1.21	7.21	1.56
C11	Visean	Al_2O_3	20.11	0.96	0.47	0.21	57.57	2.37	2.41	0.31	0.15	0.03	3.84	0.43	0.60	0.08	0.64	0.77	5.22	1.63
C12	Visean	Al_2O_3	17.19	1.33	5.58	1.47	48.37	2.89	4.38	1.33	0.08	0.02	3.14	0.47	0.53	0.10	3.21	0.93	6.32	0.97
C13	Visean	Al_2O_3	18.94	2.94	1.32	0.55	42.11	3.18	2.85	0.79	0.14	0.05	3.78	0.43	0.68	0.12	3.49	3.66	9.77	2.16
Av. Cala Mica	Visean	Al_2O_3	20.55	6.19	7.66	9.72	44.50	9.36	2.91	1.80	0.12	0.04	3.73	1.14	0.60	0.19	1.69	2.04	7.15	2.21
Breggia Gorge	Pliensbachian- Toarcian	CaO	6.15	0.36	36.67	1.76	18.86	1.77	1.44	0.55	0.05	0.01	1.46	0.02	0.32	0.01	0.05	0.01	2.38	0.14
Pale Vallone	Toarcian	CaO	6.44	0.68	35.10	2.80	20.45	1.95	1.40	0.20	0.08	0.01	2.29	0.25	0.35	0.04	0.03	0.00	3.27	0.36
Valdorbia	Toarcian	CaO	6.47	2.79	33.70	7.62	22.27	9.28	1.48	0.19	0.10	0.03	2.28	0.92	0.36	0.14	0.02	0.00	3.55	1.61
Mazak	Cenomanian	Al_2O_3	19.18	1.38	0.50	0.20	67.58	1.54	–	–	–	–	–	–	–	–	–	–	–	–
Brandenberg	Cenomanian- Turonian	CaO	10.41	1.13	26.99	3.16	26.70	2.05	4.68	1.29	0.07	0.02	3.71	0.25	0.30	0.05	0.09	0.00	5.12	0.64
Manganotone	Turonian	Al_2O_3	22.54	1.25	1.30	1.08	65.03	0.92	2.06	0.07	0.23	0.02	6.40	0.63	0.68	0.08	0.06	9.59	9.56	1.56
Trzemesnia	Turonian	Al_2O_3	17.16	1.34	0.74	0.07	65.31	1.67	1.63	0.10	0.09	0.02	4.51	0.48	0.53	0.05	0.04	0.04	6.72	1.97
Vispi	Turonian	CaO	0.06	0.02	53.09	1.16	3.47	1.33	0.38	0.03	0.05	0.02	0.23	0.06	0.02	0.00	0.06	0.01	0.26	0.14
Buchberg	Turonian	CaO	8.73	1.95	31.52	4.25	28.64	4.77	1.28	0.20	0.11	0.05	1.31	0.41	0.33	0.08	0.04	0.01	2.79	0.99
Karpenision	Santonian	Al_2O_3	8.73	3.06	10.77	13.50	53.09	7.72	–	–	–	–	–	–	0.48	0.28	0.22	0.01	7.66	4.78
Plaka	Santonian	SiO_2	0.91	0.60	12.49	23.48	73.52	38.55	–	–	–	–	–	–	0.23	0.37	0.08	0.08	0.53	0.29
Rehkogel	Santonian	CaO	8.65	0.87	32.85	2.55	26.25	2.76	1.16	0.13	0.07	0.00	1.47	0.20	0.32	0.03	0.05	0.00	3.15	0.41
Padbeh	Paleogene	CaO	3.54	1.30	36.01	7.07	20.86	7.36	2.50	1.05	–	–	0.58	0.20	0.25	0.13	0.05	0.01	2.50	1.05
Pacific red clay	Recent	Al_2O_3	16.60	–	0.70	–	54.90	–	3.40	–	0.25	–	2.70	–	0.78	–	0.56	–	7.70	–
Average shale (1971)	–	–	16.7	–	58.9	–	58.9	–	2.6	–	0.78	–	58.9	–	0.78	–	0.11	–	6.9	–
Average shale (1961)	–	–	15.12	–	3.09	–	15.62	–	2.49	–	0.16	–	3.20	–	0.77	–	0.11	–	6.75	–
Average carbonate	–	–	0.79	–	42.30	–	5.13	–	7.79	–	0.09	–	0.33	–	0.07	–	0.14	–	0.54	–
Deep sea carbonate	–	–	3.78	–	43.71	–	6.85	–	0.66	–	0.08	–	0.35	–	0.13	–	0.13	–	1.29	–
Deep sea clay	–	–	15.87	–	4.06	–	53.48	–	3.48	–	0.34	–	3.01	–	0.77	–	0.87	–	9.29	–
Upper continental crust	–	–	14.63	–	4.12	–	64.92	–	2.24	–	0.15	–	3.45	–	0.52	–	0.07	–	4.42	–

Table 5
Average minor element chemistry distribution for the different chemofacies from Viséan marine red beds recovered from the Cala Mica section of Menorca (Spain) and marine red bed profiles throughout the Phanerozoic (references found in Table 1) with standards; Wedepohl's (1971) average shale (a), Turekian and Wedepohl's (1961) average shale (b), average carbonate, deep-sea clay and deep-sea carbonate, and Wedepohl's (1995) average upper continental crust.

Section/chemofacies	V		Cr		Cu		Zn		Rb		Sr		Zr		Pb	
	ppm	Stdev	ppm	Stdev	ppm	Stdev	ppm	Stdev	ppm	Stdev	ppm	Stdev	ppm	Stdev	ppm	Stdev
C1	53.38	36.03	30.11	7.83	330.40	183.18	71.22	28.33	13.96	8.87	357.50	71.17	24.21	13.23	25.72	12.66
C2	125.57	19.35	66.92	6.82	66.94	56.57	100.03	12.60	127.46	7.60	207.42	31.42	122.18	16.38	21.23	6.99
C3	94.42	13.58	56.95	5.63	77.18	107.65	92.61	14.11	95.65	8.52	235.06	67.33	88.70	10.93	23.39	4.25
C4	81.69	32.06	41.75	2.50	92.01	72.21	78.45	7.47	56.57	9.80	251.10	11.01	55.24	12.25	23.49	11.05
C5	118.92	14.90	65.96	3.86	126.43	154.93	129.70	19.24	100.35	7.63	378.83	50.30	112.41	10.27	19.49	8.76
C6	143.36	12.44	87.80	9.31	47.25	9.74	115.04	13.18	159.89	18.24	180.49	14.63	134.41	15.57	27.12	8.58
C7	200.05	43.84	109.96	10.47	86.26	152.34	106.27	20.12	220.26	7.80	168.15	36.24	184.04	26.29	20.17	3.53
C8	171.28	25.37	100.29	7.43	55.16	31.46	108.22	15.54	208.36	8.70	163.81	21.71	171.63	10.35	23.81	4.10
C9	142.07	13.90	91.55	9.63	44.84	6.19	110.56	11.65	183.15	11.97	216.25	139.84	172.88	44.05	29.29	15.63
C10	144.37	36.80	74.17	9.67	63.32	30.84	98.62	34.90	180.71	8.83	271.93	67.02	204.50	17.21	32.16	16.33
C11	148.19	31.02	67.67	6.14	101.01	127.54	66.91	21.98	183.98	20.10	360.25	150.31	214.81	44.28	25.84	10.31
C12	135.95	31.16	67.66	5.36	117.99	107.13	114.87	19.63	145.35	20.27	316.83	98.62	163.22	35.36	25.77	10.92
C13	162.55	29.94	91.86	13.40	44.58	20.98	118.28	33.80	185.89	26.90	291.47	106.47	188.22	24.73	33.67	10.71
Av. Cala Mica	150.48	47.85	82.92	23.31	85.72	115.49	101.89	25.86	169.24	53.88	238.63	107.56	160.26	52.77	24.74	9.97
Pale Vallone	55.00	1.00	35.00	3.00	10.00	1.00	46.50	0.50	50.00	10.00	213.50	28.50	62.00	15.00	3.00	1.00
Valdorbia	64.00	18.40	44.33	14.34	13.67	4.64	49.00	14.97	57.33	20.68	219.00	23.37	62.00	27.07	0.67	0.47
Mazak	112.06	26.77	68.94	6.05	68.08	41.42	84.74	32.83	130.81	18.14	77.41	13.35	94.73	20.49	23.00	7.81
Brandenberg	33.98	38.84	62.98	82.20	10.59	7.97	29.24	27.32	35.31	43.94	414.83	149.11	70.33	5.76	10.03	4.01
Manganotone	–	–	75.02	12.00	53.75	10.12	102.38	8.88	193.71	28.69	166.51	40.41	159.40	14.00	–	–
Trzemesnia	–	–	76.31	17.00	131.08	163.61	80.92	17.70	112.31	19.22	114.69	10.20	–	–	45.15	46.60
Vispi	61.31	9.80	7.77	2.42	9.89	6.99	52.31	4.80	67.06	10.74	449.72	21.76	43.53	5.16	3.27	1.50
Buchberg	91.44	106.91	53.85	23.39	87.07	62.48	54.84	13.40	54.33	17.01	376.78	35.42	38.65	10.74	10.53	1.82
Rehkogel	5.46	2.71	50.54	9.08	18.06	1.61	17.24	8.62	–	–	492.34	71.10	3.00	1.57	11.94	0.27
Padbeh	–	–	–	–	13.62	6.26	–	–	–	–	–	–	–	–	1.92	0.66
Pacific red clay	117.00	–	64.00	–	230.00	–	165.00	–	–	–	710.00	–	–	–	34.00	–
Average shale (1971)	130	–	130	–	130	–	95	–	140	–	300	–	160	–	22	–
Average shale (1961)	130.00	–	90.00	–	45.00	–	95.00	–	140.00	–	300.00	–	160.00	–	20.00	–
Average carbonate	20.00	–	11.00	–	4.00	–	20.00	–	3.00	–	610.00	–	19.00	–	9.00	–
Deep sea carbonate	20.00	–	11.00	–	30.00	–	35.00	–	10.00	–	2000.00	–	20.00	–	9.00	–
Deep sea clay	120.00	–	90.00	–	250.00	–	165.00	–	11.00	–	180.00	–	150.00	–	80.00	–
Upper continental crust	53.00	–	35.00	–	14.30	–	52.00	–	110.00	–	316.00	–	237.00	–	17.00	–

shale and upper continental crust except for Brandenburg, which has an elevated MgO content (Fig. 11A). The second trend is strongly negative against Al_2O_3 and includes only Menorcan MRB chemofacies (C5, C10, C11, C12, C13 as well as C1) indicating that the source of MgO within these chemofacies differs from anything previously known to occur within MRBs. Recent Pacific red clays plot closely with average deep-sea clay between the two trends whilst all values plot above deep-sea carbonate apart from the Vispi section, chemofacies C1 most closely plots with the average carbonate of Turekian and Wedepohl (1961). SiO_2 forms a weak positive correlation overall against Al_2O_3; two groups of high Al, high Si (>15 wt% Al_2O_3, >40 wt% SiO_2), and low Al, low Si (<15 wt% Al_2O_3, <40 wt% SiO_2) can be distinguished (Fig. 11B). The Plaka section that is comparatively enriched in SiO_2 and depleted in Al_2O_3 and the Vispi section, depleted in both SiO_2 and Al_2O_3, form outliers, whilst chemofacies C2, C5 and the Karpenision section form intermediates between the two groups. Generally, all values plot above average carbonate, shale, and deep-sea carbonate and the first high Al, high Si group plots more closely with deep-sea clay and recent Pacific red clay. Values of P_2O_5 correlate positively with Al_2O_3, outliers from the Manganotone section and recent pacific red clays plot above the standards (Fig. 11C). Generally, MRBs plot below the standard values of P_2O_5 against the trend suggesting an overall lower bioproductivity. Values of K_2O correlate positive with Al_2O_3, whereas CaO depicts two negative trends as seen before (Fig. 11D and E). The more negative CaO trend correlates more with the average carbonate and the deep-sea carbonate whereas the lower CaO wt% trend plots close to average shale, deep-sea clay and the upper continental crust as well as the recent Pacific red clay. Values of TiO_2 form a very strong positive correlation, again indicating TiO_2 is occurring solely within the terrigenous fraction (Fig. 11F). Its concentration is depleted relative to recent Pacific red clay, average shale and deep-sea clay. There is noticeably more scatter within the Ca-MRB cluster suggesting greater variation in aeolian input and/or greater changes within the paleoenvironmental energy regime for Ca-MRBs (Spofforth et al., 2008; Tisserand et al., 2009; Ziegler et al., 2008). Values of MnO within all published MRB datasets are low (below 1 wt% MnO) (Fig. 11G), indicating a separate external source of MnO like for the aforementioned MgO values, which has not been acknowledged thus far in MRBs. Fe_2O_3T values correlate positive with Al_2O_3 indicating that Fe mostly resides in the terrigenous fraction and generally plots with all standards, slightly greater scatter is seen with increasing Al_2O_3 concentrations (Fig. 11H). When considered in terms of their respective geochemical MRB-endmember, then most Menorcan MRB-chemofacies can be classified as Al-MRBs and are geochemically very similar to the Manganotone, Trzemesnia, and Mazak MRBs (Fig. 11I). Except for chemofacies C3 which is more geochemically similar to the Brandenburg section MRBs that plot close to the border between Ca-MRB and Al-MRB endmembers. Chemofacies C4 is geochemically most similar to the Ammonitico Rosso facies from the Pale Vallone, Valdorbia and Breggia Gorge sections. Chemofacies C1 can be considered as geochemically unique and is the closest to a mixture of all three endmembers. Al-MRBs are most similar to the average deep-sea clay and the upper continental crust, although Menorcan MRBs on average plot between the deep-sea clay and the average shale of Turekian and Wedepohl (1961) and Wedepohl (1995). Ca-MRBs cluster slightly and plot below deep-sea carbonate around 40 wt% CaO, 50 wt% Al_2O_3 and 20 wt% SiO_2, with the exception of the Vispi section that is enriched relative to the average carbonate. From the data available it can be stated that Si-MRBs are very uncommon, with the only current example being the Plaka section of CORBs (Hu et al., 2012).

4.3.2. Minor elements

Values of V correlate positively with Al_2O_3, are enriched relative to the upper continental crust and the deep-sea clay except for the

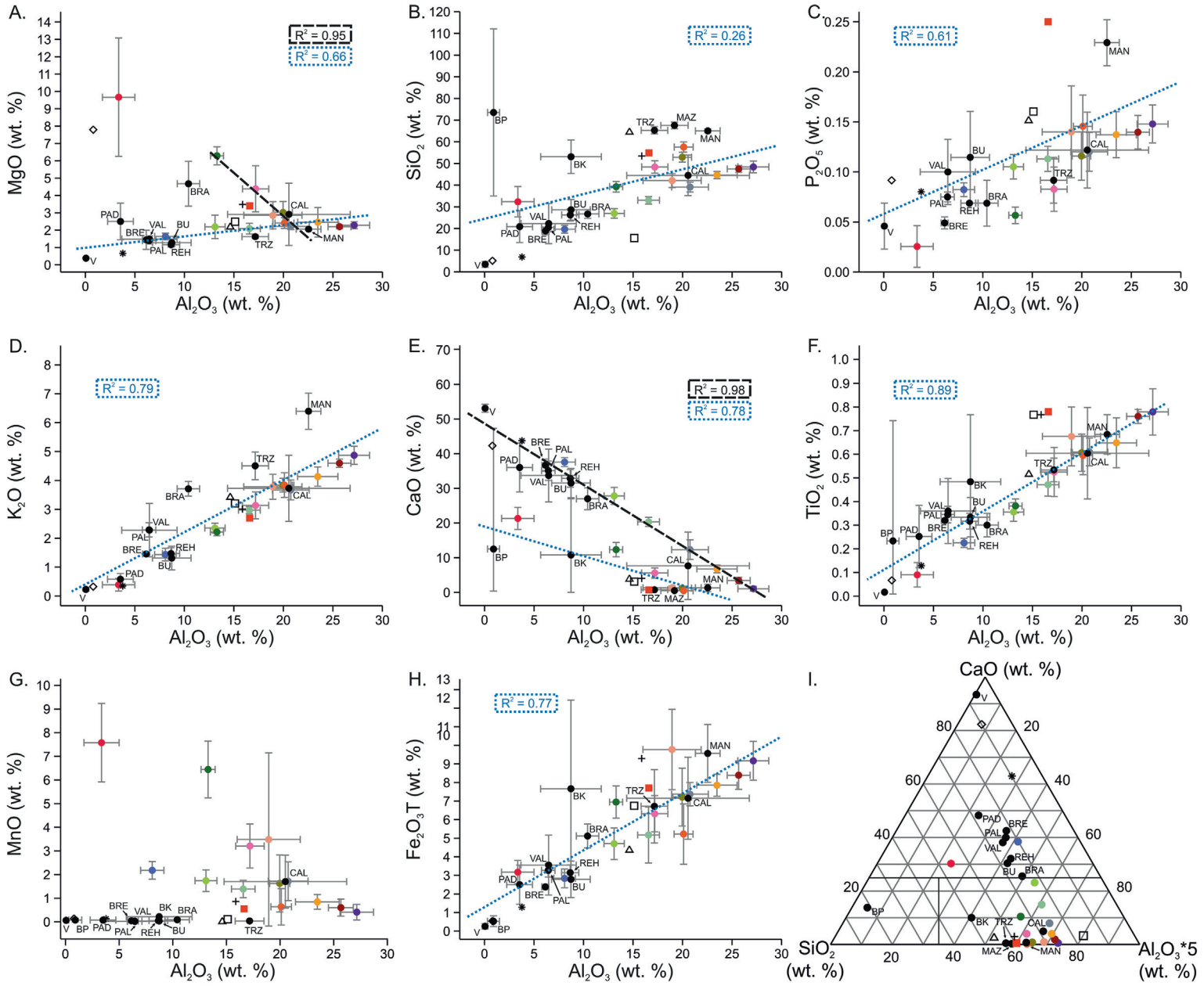

Fig. 11. Major elements of marine red beds throughout the Phanerozoic and chemofacies from Viséan marine red beds recovered from the Cala Mica section of Menorca (Spain) plotted against Al_2O_3. Standards are taken from Turekian and Wedepohl (1961) and Wedepohl (1995): square = average shale, diamond = average carbonate, star = deep-sea carbonate, plus = deep-sea clay, triangle = average composition of the upper continental crust. MRB profiles: AIZ = Aizpute, BK = Karpenision, BP = Plaka, BRA = Brandenberg, BRE = Breggia Gorge, BU = Buchberg, CAL = Cala Mica, MAN = Manganotone, MAZ = Mazak, PAD = Padbeh, PAL = Pale Vallone, QUE = Quebec, REH = Rehkogel, TRZ = Trzemesnia, V = Vispi, VAL = Valdorbia. The references for the discussed MRB profiles can be found in Table 1. (For interpretation of the references to colour in this figure legend, the reader is referred to the web version of this article.)

Brandenburg and Rehkogel sections. Again, two distinct clusters are formed by the Ca-MRBs and the AL-MRBs (Fig. 12A). This is similar to the values of Cr that correlate strongly positive with Al_2O_3, plotting succinctly between the upper continental crust, deep-sea carbonate, the average carbonate, the average shale, and the deep-sea clay with the exception of the Cr-depleted Vispi section (Fig. 12B). Cu shows no affinity to the terrigenous fraction; on average Al-MRBs have greater concentrations of Cu than Ca-MRBs, although all values are depleted relative to the deep-sea clay and the recent Pacific red clays with the exception of chemofacies C1 (Fig. 12C). Zn forms two distinct clusters of Ca-MRBs and Al-MRBs when plotted against Al_2O_3, highlighting the diluting effect of biogenically precipitated carbonate (bioproductivity) upon the terrigenous supply (Fig. 12D). Within their respective clusters, the Menorcan MRB-chemofacies is generally enriched in Zn compared to other MRB-examples. Values of Rb for MRBs correlate strong positive with Al_2O_3, with Ca-MRBs plotting at the low-end and Al-MRBs at the high-end and chemofacies C3 and C5 acting as intermediates (Fig. 12E). Sr exhibits a weak negative correlation with Al_2O_3, showing a more scattered negative trend suggesting again that Sr is residing in different phases in different quantities outside the terrigenous fraction (Fig. 12F). Recent Pacific red clay has a substantially elevated Sr content compared to ancient MRBs, this can be attributed to the presence of celestite skeletons produced by surface-dwelling acantharia which are not preserved in the fossil record due to celestite dissolution with respect to extremely under saturated ocean waters (Brass and Turekian, 1974; Brass, 1980). Values of Zr positively correlate with Al_2O_3 (Fig. 12G), whereas Pb doesn't show any particular correlation. The Ca-MRB chemofacies from Menorcan MRBs show a relative enrichment of Pb compared to other Ca-MRB examples (Fig. 12H). The Trzemesnia section contains the highest quantity of Pb out of all examples, due to the presence of a siliceous-manganese variegated shale unit, which is 1.2 m thick and contains ferromanganese crust horizons that provided an additional external source of Pb outside of the sedimentary system (Bąk, 2007; Neuhuber and Wagreich, 2009).

5. Discussion

5.1. Comments on the origin of the red coloration in Menorcan marine red beds

From microscopic data the red color within Menorcan MRBs can be attributed to the presence of homogenously dispersed iron-rich phases within the clay-sized terrigenous fraction. Iron oxides such as hematite are considered to be the controlling parameter for the red color within MRBs (Lajoie and Chagnon, 1973; Ziegler and McKerrow, 1975; Kiipli et al., 2000; Hu et al., 2009), although the Fe_2O_3T contents of Menorcan MRBs display no particular enrichment but are very similar to that of Wedepohl's (1971) average shale (total average $EF_{Fe} = 0.84$). A similar pattern can be seen across other MRB occurrences whereby concentrations of Fe_2O_3T positively correlate with Al_2O_3 within the terrigenous fraction and plot with the standards ($R^2 = 0.77$). This has been known and considered for some time in many Type-I and Type-II MRB studies, where a simple enrichment of Fe doesn't necessarily impart the red color in MRBs, such as Lajoie and Chagnon's (1973) red claystones, which contain approximately similar concentrations of Fe_2O_3 as their green claystones (8 wt%), but higher Fe/Mn ratios and greater quantities of hematite and chamosite. The red color in red beds is not controlled by an elevated iron content – very low iron oxide concentrations of <1 wt% are already sufficient to stain a sediment red (He et al., 2022). The red color appears to be dependent upon the size, distribution and crystallinity of the iron-oxide particles, which is largely controlled by diagenetic processes; for hematite the red color decreases when either the degree of hematite crystallinity or the grain size of the hematite particle increases (Hund, 1966; Cai et al., 2008; Li and Cai, 2013).

Typically, Mn-bearing mineral phases such as rhodochrosite are considered to have an additional effect upon the red color in some examples of red limestones that have not undergone extensive diagenesis (Ca-MRBs) and are not typically attributed as red coloring agents for red shales (Al-MRBs) (Calderoni and Ferrini, 1984; Cai et al., 2009; Li et al., 2011). With an average of 1.69 wt% MnO, Menorcan MRBs are consistently enriched compared to Wedepohl's (1971) average shale (average $EF_{Mn} = 12.48$) and contain considerably higher MnO concentrations than any MRB used in this study for comparison. The most similar example being red calcareous mudstones from the top of the Santonian-aged Karpenision section which contains on average 0.22 wt% MnO, Baltuck (1982) attributes this to subaerial exposure of ophiolitic material in the northeast of the Pindos Basin that introduced an 'oceanic' component to the sediments. There are elemental indicators preserved within the Menorcan MRBs that may point to a hydrothermal source such as a moderate enrichment of Cu, Sr and Pb within the more siliceous and calcareous chemofacies. Additionally, hydrothermal activity is regarded to be a critical component in the formation of phosphate nodules (Gao et al., 2018). The presence of phosphate nodule containing strata underlying the MRBs (Bourrouilh and Termier, 1973) may therefore also point towards paleohydrothermal activity. Typically, 70–80 % of Mn-bearing minerals within deep-sea sediments can be attributed to hydrothermal activity, which later undergo alteration during the processes of early diagenesis (Rothwell and Croudace, 2015). It is known that under oxidizing conditions at the sediment-seawater interface, (such is the case for MRB formation) $MnCO_3$ precipitation in the form of rhodochrosite occurs as a result of the downward diffusion of Mn^{2+} due to the dissolution of oxyhydride particles (MnO_2 and MnOOH) (Pedersen and Price, 1982; Brumsack, 1989; Rajendran et al., 1992; Calvert and Pedersen, 1993; Caplan and Bustin, 1999; Morford et al., 2001; Tribovillard et al., 2006) as well as the reaction with organic and sulfide phases (Huerta-Diaz and Morse, 1992; Algeo and Maynard, 2004). Whereas under anoxic conditions upward diffusion of Mn^{2+} occurs, enabling Mn^{2+} to escape to the water column resulting in relative depletion (Hild and Brumsack, 1998; Cruse and Lyons, 2004).

A greater bright reddened staining is present within MRBs that contain a larger calcitic biogenic component, although no substantial coloration could be observed in thin sections within the interstices of calcite microlites or calcite grains as previously documented in CORB red limestones (Hu et al., 2012). There, iron was thought to be trapped within the calcite structure and subsequently replaced oxygen from the CaO_6 octahedron to form $Fe_2O_3^{2-}$ clusters that were oxidized to form hematite (Cai et al., 2009). Within Menorcan red pelagic limestones the red staining seems to be more closely associated with the surrounding calcareous clay fraction, supporting a detrital mode of origin for the fossilized material, as given by the abundance of partially disarticulated crinoid stems within these deposits. Suggesting the 'brightened red' color could be a result of 'color dilution' from the calcitic biogenic material that has been carried in periodically and deposited within the red mudstone background sedimentation. The presence of iron coccoid-like clusters and geometries within the red mudstone facies of Menorcan MRBs could point to the activity of Fe-fixing bacteria and their contribution towards the coloration of MRBs. However, it is known that iron-bacteria are eliminated under highly oxidizing conditions (Fenchel and Finlay, 1995; Préat et al., 2018), which may rule-out iron-bacteria as an important contributor for the red staining. Préat et al. (2006) suggested a mechanism for the Ammonitico Rosso facies, where the presence of dysoxic to anoxic bottom-water conditions inhibited the spread of burrowers and subsequently prevented the colonization with iron-oxidizing biofilms which ultimately form hematite. However, the values of the redox sensitive elements V and Cr within Menorcan MRBs do not give a clear indication of anoxic conditions present at the time of deposition. Furthermore, more and different redox proxies will have to be used to constrain the redox history of these MRBs.

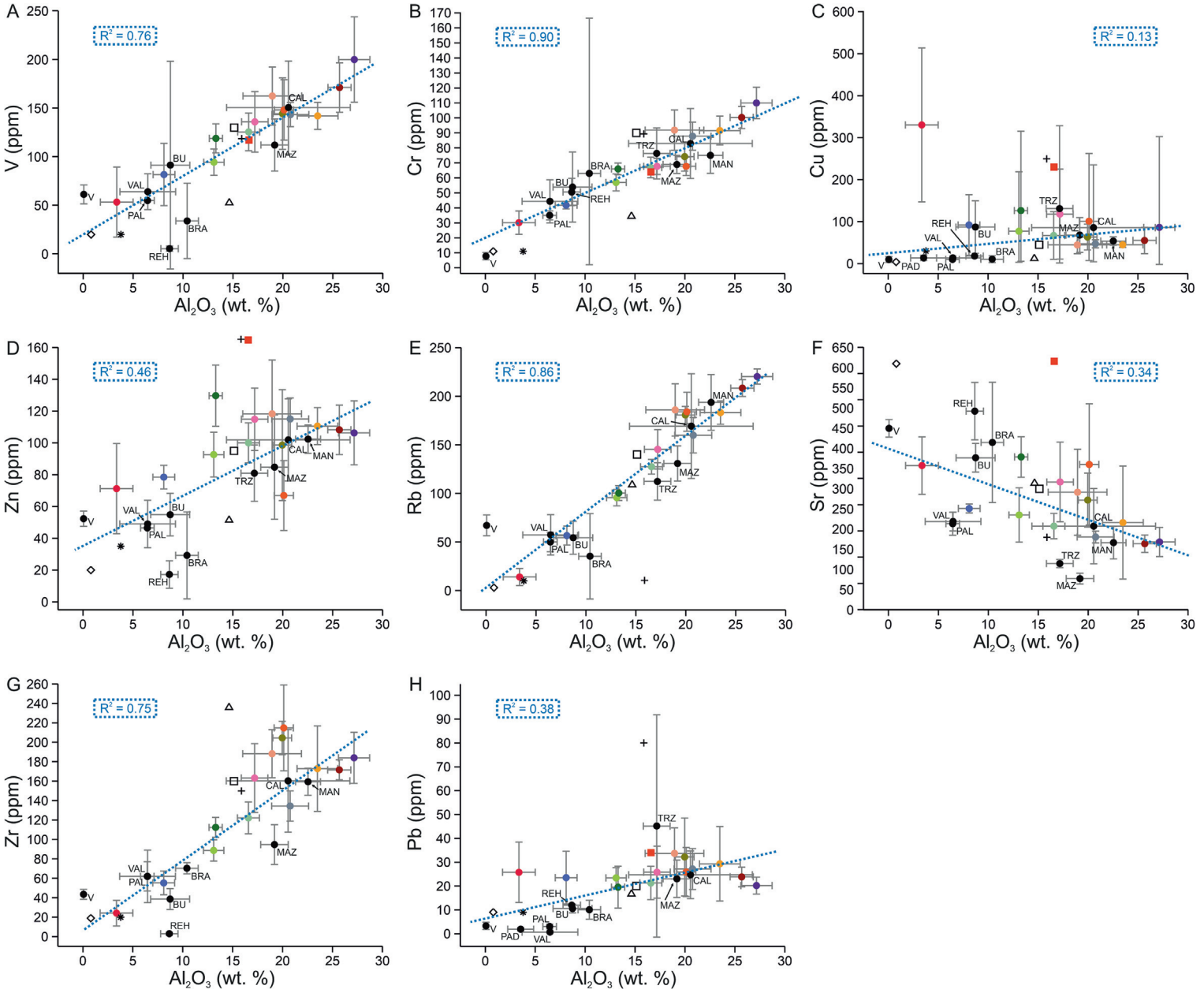

Fig. 12. Minor elements of marine red beds throughout the Phanerozoic and chemofacies from Viséan marine red beds recovered from the Cala Mica section of Menorca (Spain) plotted against Al_2O_3. Standards are taken from Turekian and Wedepohl (1961) and Wedepohl (1995): square = average shale, diamond = average carbonate, star = deep-sea carbonate, plus = deep-sea clay, triangle = average composition of the upper continental crust. MRB profiles: AIZ = Aizpute, BK = Karpenision, BP = Plaka, BRA = Brandenberg, BRE = Breggia Gorge, BU = Buchberg, CAL = Cala Mica, MAN = Manganotone, MAZ = Mazak, PAD = Padbeh, PAL = Pale Vallone, QUE = Quebec, REH = Rehkogel, TRZ = Trzemesnia, V = Vispi, VAL = Valdorbia. Original references for discussed MRB profiles can be found in Table 1. (For interpretation of the references to colour in this figure legend, the reader is referred to the web version of this article.)

5.2. Origin of Early Carboniferous Menorcan MRBs: widespread oxygenation of the Western Paleotethys Ocean

Radiolarian chert sedimentation was particularly widespread in the Early Carboniferous (Engel et al., 1982; Raymond and Lethiers, 1990; Raymond and Caridroit, 1994; Gursky, 1996; Gursky, 1997; Wajsprych and Achramowicz, 2003; O'Dogherty et al., 2000; Krainer and Vachard, 2015), due to a marked paleoceanographic homogenization in most European marine basins, the so-called 'bathyal lull' of Goldring (1962), just before the onset of the Variscan orogeny (O'Dogherty et al., 2000). O'Dogherty differentiates between two regions and types of chert units across western and central Europe, [1] sequences of hemipelagic and pelagic sediments with radiolarian cherts that grade into graywacke flysch deposits of the developing Variscan Orogeny (Germany, South Portugal, Montagne Noire, Eastern Alps), that lay basinward of the Laurussian fringing carbonate shelfs. [2] Gondwanan-derived microcontinental blocks (Alboran-Kabylian-Peloritan-Calabrian terrane) with basins to the north of the Betic-Rif block (Herbig, 1989), which contain cherts representing a pelagic interval within a variable succession of mostly shelf and slope limestones (Cantabrian Zone, Malaguide Complex). Radiolarian chert sedimentation is also seen directly beneath the MRBs on Menorca, although the occurrence of MRBs following periods of siliceous deposition at this time interval is poorly understood and recognized. The Early Carboniferous succession of Menorca is generally considered to be Gondwanan-derived due to its apparent location somewhere in the Alboran-Kabylian-Peloritan-Calabrian terrane. Based on similar sedimentological characteristics to the Chenoua massif of Algeria and the Khudiat Tizan internal rif of the Moroccan nappes (Bourrouilh, 2016). Although Herbig (1994) noted the close relation and potential palaeogeographical relationship between the crinoids *Balearocrinus breimeri* from the MRBs of Menorca and *Balearocrinus cantabricus* in the griotte facies of the Genicera Formation (Upper Tournaisian - Lower Namurian) of the Cantabrian Mountains, Northern Spain. Such a relationship would support the hypothesis of an influx of detrital material into the Late Viséan Menorcan sedimentary system from the northern Iberian chain. The Alba griotte Formation, also located within the Cantabrian Mountains is comprised of thin-bedded, red and gray nodular limestones and radiolarites deposited at the Viséan -Namurian boundary that thickens south of the León-Line (Kullmann and Schönenberg, 1978), although the relationship between these deposits and the MRBs of Menorca have not yet been studied. The hypothesis of further MRB deposits across this time interval throughout the western Mediterranean hints at the possibility of well-established oxygenated conditions within the most northern section of the Western Paleotethys at the time of general basin homogenization during the bathyal lull. Alternatively, the poor documentation of MRBs from the Late Viséan proposes that their existence was basin exclusive during the onset of the Variscan orogenesis similar to what has been proposed for CORB deposits that are considered more so as localized deposits in deep water, oceanic basins, far from shorelines and vestiges of a widespread oceanic oxygenation event (Wang et al., 2005; Wang et al., 2009; Wagreich et al., 2009). Similar conclusions have been reached from a horizon of late Pragian to earliest Emsian type-I red pelagic carbonates across the Prague Basin (Czech Republic), where Bábek et al. (2018) found that MRBs only developed within the most distal parts of the basin and were strongly controlled by a low sedimentation rate ranging between 1.18 and 8.5 mm/kyr.

Menorcan MRBs within the Cala Mica section can be considered as the dominant background sedimentation following a supposed change in redox conditions from radiolarite deposition that was interrupted by external influences such as hydrothermal activity and light gray tempestitic/turbiditic limestones. Even though the interplay between these components within the succession needs to be analyzed in full and greater detail to determine the exact relationships and the nature of what appears to a dramatic change in redox conditions and possible provenance change within the deep-marine environment of the Western Paleotethys Ocean during the Late Viséan. MRBs acting as the dominant background sedimentation is also documented from Cretaceous deep-water red shales intercalated with gray turbiditic beds in the Gosau Group (Austria) (Wagreich and Krenmayr, 2005). The red pelagic carbonates in the Prague Basin are most preferentially developed during times of maximum flooding (peak transgression) and the associated sediment starvation (Koptíková et al., 2010; Bábek et al., 2018). A similar sequence stratigraphical stance could be hypothesized for Menorcan MRBs (Herbig, 1998), although the apparently cyclic occurrence of gravitationally derived light gray limestone tempestites/turbidites could suggest deposition during lowstand, the start of which could be assigned to the large 50 m thick Nivel Olistostrómico within the underlying radiolarites (Bourrouilh, 1973). However, a conclusion regarding the relative sea-level can't be reached at this point as the sequence-stratigraphic frame of the Menorcan MRBs remains to be investigated.

The occurrence of MRBs within the Cala Mica section can so far be attributed to changes in the paleoceanographic and paleoclimatologic setting, potentially the establishment of widespread oligotrophic and oxygenated bottom water conditions. The complex interplay of apparent cyclicity within the Cala Mica section between MRBs and limestone tempestites/turbidites is most likely a mixture of third order glacioeustatic sedimentary forcing as well as a larger scale orogenic influence due to the closure of the Paleotethys prior to the onset of the Variscan causing basin homogenization, although the link between MRB deposition and particular T-R trends remains vague and uncertain.

5.3. Geochemistry of Phanerozoic MRBs: relation to oceanic anoxic events (OAEs) and Menorcan MRBs

Song et al. (2017) explain that the prerequisites for MRB deposition were anoxic, ferruginous water column conditions, whereby the displacement of Fe^{2+}-enriched anoxic waters with iron concentrations greater than the average upper limit of Fe-ligand concentration in modern oceans (4 nM; Gledhill and Buck, 2012), into oxic waters caused the precipitation of hydrous ferric oxide phases that diagenetically altered to hematite. This mechanism was enabled by the transition to widespread deep ocean oxygenation in the terminal Proterozoic, differing from banded iron formations (BIFs) and MRBs from the mid-Proterozoic (Fike et al., 2006; Canfield et al., 2008), which promoted MRB deposition following ocean anoxia. Although, the slight enrichment of Fe is contentiously preserved within MRBs as a result of OAE's given by the geochemical data compiled and presented in this study. The same was found for the Late Devonian red pelagic limestones from the Prague Basin by Bábek et al. (2018) which favored global cooling and high atmospheric pO_2 levels that led to a higher concentration of dissolved oxygen in the deep, cold waters and therefore to the diagenetic formation of MRBs, similar to CORBs (Wang et al., 2011; Hu et al., 2012). Additionally, lower rates of silicate weathering together with oligotrophic conditions resulting in reduced organic input caused a diminished oxygen consumption in the top sediments during the early diagenesis (Bábek et al., 2018). This effect could also be associated with times following a period of organic carbon deficit caused by increased carbon retention in the sediment, e.g., during oceanic anoxic events and the associated black shale deposition.

The chemofacies derived from Menorcan MRBs provided a successful means to compare the sub-lithofacies-scale heterogeneity of these MRB successions to other MRB occurrences throughout the Phanerozoic and published standard values. Values of K_2O, TiO_2, and Fe_2O_3T within MRBs plot positively with Al_2O_3, regardless of the MRB-endmember. However, MRBs preferentially cluster as Ca- and Al-endmembers with regards to the heavy mineral phases as it is demonstrated by the TiO_2, Zn, and Zr concentrations. The CaO values within more siliceous MRBs are lower than for Ca-MRBs and generate different trends, but generally higher compared to Al-MRBs. This is tentatively interpreted here to be a result of elevated bioproductivity, leading to a mixture between carbonate- and siliceous biogenic components. But Si-MRBs are rare, and more data are required to validate such an interpretation. MgO values within MRBs correlate lightly with the terrigenous fraction as do the MgO concentrations of the Ca-MRBs from Menorca, whereas MRBs with

higher SiO_2 and Al_2O_3 from Menorca do not. P_2O_5 within MRBs also mostly resides within the terrigenous fraction, detrital P_2O_5 is most often associated with apatite derived from a range of provenance sources (Belousova et al., 2002; Morton and Yaxley, 2007), as well as within clay fractions and iron oxides whereby the greater surface heterogeneity, larger surface site density and smaller particle size results in a stronger P adsorption capacity (Fang et al., 2017). The predominantly terrigenous nature of P within MRBs suggests a low primary productivity during the time of their formation. Redox sensitive elements within the MRBs plot with the V-values and slightly below the Cr-values of the standards used for comparison. Under pelagic and hemipelagic conditions, vanadium is tightly coupled with the redox cycle of Mn (Hastings et al., 1996; Tribovillard et al., 2006), whereas in oxic waters V is present as vanadate which can readily adsorb onto Mn- and Fe-oxyhydroxides (Calvert and Piper, 1984; Wehrly and Stumm, 1989; Tribovillard et al., 2006). It has to be noted, however, that the absence of an expected V-enrichment is not necessarily indicative of more oxic conditions. Cr concentrations within MRBs are depleted relative to average shale and deep-sea clay and correlate strongly with the terrigenous fraction across all MRB endmembers, whilst Ca-MRBs plot above carbonate standards with the exception of the Valdorbia section. Cr occurs as Cr(VI) in oxygenated seawater as the soluble chromate anion (CrO_4^{2-}). The general depletion in Cr in most Al-rich MRBs suggests an increased solubility of Cr within the seawater at the time of deposition, which may indicate more oxygenated conditions. The micronutrient elements Cu and Zn do not show any particular depletion or enrichment for MRBs and tend to plot with the standards.

6. Conclusions

A Late Viséan section hosting MRBs from northern Menorca (Balearic Islands, Spain) is considered to be a remnant of the Western Paleotethyan Alboran-Kabylian-Peloritan-Calabrian terrane. The Menorcan MRB-succession is comprised of the three distinctive MRB lithofacies [1] red mudstone (Rmu), [2] red pelagic limestone (Rpl), and [3] red silty mudstone (Rsm) together with cyclic light-gray limestone tempestite/turbidite deposits. The MRB lithofacies are interpreted to represent the dominant background sedimentation following a period of predominantly radiolarite formation. This transition from radiolarite formation to MRB deposition is considered to be associated with a change in the redox conditions of the water column.

The different MRB lithofacies have been analyzed by means of energy dispersive XRF and grouped into 13 distinct chemofacies using hierarchical cluster analysis. This resulted in 11 Al-MRB endmembers (C2, C3, C5, C6, C7, C8, C9, C10, C11, C12, and C13) and two Ca-MRB endmembers (C1 and C4). The overall Menorcan MRB chemofacies is very similar to the chemical composition of Wedepohl's (1971) average shale, with the exception of a consistent MnO enrichment. This enrichment is interpreted to be the result of a local hydrothermal source, through which Mn-bearing fluids initiated the precipitation of Mn-minerals such as rhodochrosite. Menorcan MRBs are generally depleted in SiO_2, P_2O_5, TiO_2, and Cr, consistent with a distal, deep-marine depositional environment under oxic-suboxic, oligotrophic conditions. The Al-MRBs are depleted in MgO, CaO, Zn and Sr, and enriched in Rb relative to the Ca-MRBs. The concentrations of K_2O and TiO_2 correlate strongly positive with Al_2O_3 ($R^2 = 0.96$ and 0.82, respectively), implying that K and Ti are entirely residing within the terrigenous fraction and indicating the lack of any major diagenetic remobilization. Menorcan MRBs show two distinct trends for MgO, SiO_2, CaO and MnO versus Al_2O_3. These two trends are formed by chemofacies C2, C3, C4, C6, C7, C8, and C9 (trend 1) and C5, C10, C11, and C12 (trend 2) with C1 sometimes plotting with the second trend and C13 acting as an intermediate. The two trends are interpreted to illustrate the effect of external element sources such as biogenic carbonate (excess carbonate) and biogenic silica (excess silica), with the first trend documenting the impact of excess carbonate and the second trend a combination of excess carbonate and excess silica.

The Menorcan MRB chemofacies clusters were compared with published Phanerozoic MRB bulk geochemical data (Cambrian, Silurian, Cretaceous, Jurassic, Paleogene and modern Pacific Ocean deposits). In general, Al-MRBs and Ca-MRBs appear to be the most common type of MRBs, whilst Si-MRBs are less common. MRBs generally show low values of P_2O_5, TiO_2, Cr and Zr in comparison to Turekian and Wedepohl's (1961) average composition of shale, carbonate, deep-sea carbonate and deep-sea clay as well as Wedepohl's (1995) average composition of the upper continental crust. Fe_2O_3T dominantly occurs within the terrigenous fraction ($R^2 = 0.77$), and provides no evidence for Fe_2O_3T enrichment, emphasizing the red staining effect of homogenously dispersed hematite grains upon MRBs. The Menorcan MRB chemofacies clusters are geochemically similar to the Cretaceous MRBs from the Manganotone-, Trzemesnia-, and Mazak sections, except for chemofacies C3 which displays geochemical affinities to the Cretaceous Brandenburg section. Chemofacies C4 is geochemically very similar to the Jurassic Ammonitico Rosso facies from the Pale Vallone, Valdorbia and Breggia Gorge sections. Chemofacies C1 is geochemically unique and is the closest to a mixture of all three MRB-endmembers. Al-MRBs are most comparable to the average deep-sea clay and the upper continental crust, although Menorcan MRBs on average plot between the deep-sea clay and the average shale (Turekian and Wedepohl, 1961; Wedepohl, 1995). Ca-MRBs scatter slightly and plot below the deep-sea carbonate around 40 wt% CaO, 50 wt% Al_2O_3 and 20 wt% SiO_2, with the exception of the Cretaceous Vispi section that is enriched relative to the average carbonate of Turekian and Wedepohl (1961).

Supplementary data to this article can be found online at https://doi.org/10.1016/j.sedgeo.2022.106313.

Data availability

Data are provided as tables in Supplementary Material

Declaration of competing interest

The authors declare that they have no known competing financial interests or personal relationships that could have appeared to influence the work reported in this paper.

Acknowledgements

We thank the Editor-in-Chief Catherine Chagué and the reviewers Haijun Song and an anonymous reviewer for their constructive comments and suggestions, which helped us to clarify our ideas and improve the original manuscript. We acknowledge the technical support of Mr. David Wilde and Mr. Peter Greatbatch (Geography, Geology and the Environment, GGE, Keele University, U.K.) in analytical sample preparation and thin section generation. This research did not receive any specific grant from funding agencies in the public, commercial, or not-for-profit sectors.

References

Agnihotri, R., Altabet, M.A., Herbert, T.D., Tierney, J.E., 2008. Subdecadally resolved paleoceanography of the Peru margin during the last two millennia. Geochemistry, Geophysics, Geosystems 9, 1–15.

Alassane, A., Trabelsi, R., Dovonon, L.F., Odeloui, D.J., Boukari, M., Zouari, K., Mama, D., 2015. Chemical evolution of the continental terminal shallow aquifer in the South of Coastal Sedimentary Basin of Benin (West-Africa) using Multivariate factor Analysis. Journal of Water Resource and Protection 7, 496–515.

Algeo, T.J., Maynard, J.B., 2004. Trace-element behavior and redox facies in core shales of Upper Pennsylvanian Kansas-type cyclothems. Chemical Geology 206, 289–318.

Arthur, M.A., Fischer, A.G., 1977. Upper Cretaceous–Paleocene magnetic stratigraphy at Gubbio, Italy I. Lithostratigraphy and sedimentology. Geological Society of America Bulletin 88, 367–389.

Azema, J., Bourrouilh, R., Champetier, Y., Fourcade, E., Rangheard, Y., 1974. Rapports stratigraphiques, paleogeographiques et structuraux entre la Chaine iberique, les

Cordilleres betiques et les Baleares. Bulletin de la Société Géologique de France 7, 140–160 (in French with English abstract).
Bábek, O., Faměra, M., Hladil, J., Kapusta, J., Weinerová, H., Šimíček, D., Slavík, L., Ďurišová, J., 2018. Origin of red pelagic carbonates as an interplay of global climate and local basin factors: insight from the lower Devonian of the Prague Basin, Czech Republic. Sedimentary Geology 364, 71–88.
Bábek, O., Kumpan, T., Calner, M., Šimíček, D., Frýda, J., Holá, M., Ackerman, L., Kolková, K., 2021a. Redox geochemistry of the red 'orthoceratite limestone' of Baltoscandia: possible linkage to mid-Ordovician palaeoceanographic changes. Sedimentary Geology 420, 105934. https://doi.org/10.1016/j.sedgeo.2021.105934.
Bábek, O., Vodrážková, S., Kumpan, T., Kalvoda, J., Holá, M., Ackerman, L., 2021b. Geochemical record of the subsurface redox gradient in marine red beds: a case study from the Devonian Prague Basin, Czechia. Sedimentology 68, 3523–3548.
Bąk, K., 2007. Deep-water facies succession around the Cenomanian–Turonian boundary in the Outer Carpathian basin: sedimentary, biotic and chemical records in the Silesian Nappe, Poland. Palaeogeography, Palaeoclimatology, Palaeoecology 248, 255–290.
Baltuck, M., 1982. Provenance and distribution of Tethyan pelagic and hemipelagic siliceous sediments, Pindos Mountains, Greece. Sedimentary Geology 31, 63–88.
Baud, A., 2013. The Olenekian (early Triassic) Red Ammonoid Limestone, a time-specific facies on the Gondwana margin: Timor - Roof of the World - Oman connection. Acta Geologica Sinica - English Edition 87, 894–931.
Belousova, E.A., Griffin, W.L., O'Reilly, S.Y., Fisher, N.I., 2002. Apatite as an indicator mineral for mineral exploration: trace-element compositions and their relationship to host rock type. Journal of Geochemical Exploration 76, 45–69.
Bischoff, J.L., Heath, G.R., Leinen, M., 1979. Geochemistry of deep-sea sediments from the Pacific manganese nodule province: DOMES Sites a, B, and C. In: Bischoff, J.L., Piper, D. Z. (Eds.), Marine Geology and Oceanography of the Pacific Manganese Nodule Province. Springer, Boston, MA, pp. 397–436.
Bouillin, J.P., Durand-Delga, M., Olivier, P., 1986. Betic-Rifian and Tyrrhenian arcs: distinctive features, genesis and development stages. In: Wezel, F.C. (Ed.), The Origin of Arcs. Elsevier, Amsterdam, pp. 281–304.
Bourrouilh, R., 1973. Stratigraphie, sédimentologie et tectonique de l'Ile de Minorque et du Nord-Est de Majorque (Baléares) - La terminaison nord-orientale des Cordillères Bétiques en Méditerranée occidentale. (Ph.D. thesis)Université de Paris VI, Paris (822 pp. (in French)).
Bourrouilh, R., 1983. Estratigrafía, Sedimentología y Tectónica de la isla de Menorca y del Noreste de Mallorca (Baleares). Memorias del IGME 99, 1–672 (in Spanish).
Bourrouilh, R., 2016. The Balearic Islands in the Alpine Orogeny. Boletín Geológico y Minero 127, 527–546.
Bourrouilh, R., Gorsline, D.S., 1979. Pre-Triassic fit and alpine tectonics of continental blocks in the western Mediterranean. Geological Society of America Bulletin 90, 1074–1083.
Bourrouilh, R., Termier, G., 1973. *Balearocrinus breimeri*, crinoide noveau du Viséen supérieur de Minorque (Baléares). Annales de la Societé géologique du Nordvol. 93 pp. 225–232 (in French with English abstract).
Bourrouilh, R., Lys, M., 1977. Sédimentologie et micropaléontologie d'olistostromes et coulées boueuses du Carbonifère des zones internes bético-kabylo-rifaines. Annales de la Société géologique du Nord 97, 87–94 (in French with English abstract).
Brass, G.W., 1980. Trace elements in acantharian skeletons. Limnology and Oceanography 25, 146–149.
Brass, G.W., Turekian, K.K., 1974. Strontium distribution in GEOSECS oceanic profiles. Earth and Planetary Science Letters 23, 141–148.
Breit, G.N., Wanty, R.B., 1991. Vanadium accumulation in carbonaceous rocks: a review of geochemical controls during deposition and diagenesis. Chemical Geology 91, 83–97.
Brett, C.E., McLaughlin, P.I., Histon, K., Schindler, E., Ferretti, A., 2012. Time-specific aspects of facies: state of the art, examples, and possible causes. Palaeogeography, Palaeoclimatology, Palaeoecology 367–368, 6–18.
Brumsack, H.J., 1989. Geochemistry of recent TOC-rich sediments from the Gulf of California and the Black Sea. Geologische Rundschau 78, 851–882.
Bryant, W.R., Bennet, R.H., 1988. Origin, physical, and mineralogical nature of red clays: the Pacific Ocean Basin as a model. Geo-Marine Letters 8, 189–249.
Buchroithner, M.F., Flügel, E., Flügel, H., Stattegger, K., 1980a. Die Devongerölle des paläozoischen Flysch von Menorca und ihre paläogeographische Bedeutung. Neues Jahrbuch für Geologie und Paläontologie Abhandlungen 159, 172–224 (in German with English abstract).
Buchroithner, M., Flügel, E., Flügel, H., Stattegger, K., 1980b. Mikrofazies, Fossilien und Herkunft der Kalk Gerölle im Karbon-"Flysch" der Betischen Kordilleren, Spanien. Facies 2, 1–54 (in German with English abstract).
Cai, Y.F., Li, X., Pan, Y.G., Hu, X.M., 2008. The colour causing mechanism of Mn^{2+} and Fe^{3+}: evidence from the Italian cretaceous pelagic red limestones. Acta Geologica Sinica 82, 133–138.
Cai, Y.F., Li, X., Hu, X.M., Chen, X.M., Pan, Y.G., 2009. Paleoclimatic approach to the origin of the colouring of Turonian pelagic limestones from the Vispi Quarry section (cretaceous, Central Italy). Cretaceous Research 30, 1205–1216.
Cai, Y., Hu, X., Li, X., Pan, Y., 2012. Origin of the red colour in a red limestone from the Vispi Quarry section (Central Italy): a high-resolution transmission electron microscopy analysis. Cretaceous Research 28, 97–102.
Calderoni, G., Ferrini, V., 1984. Abundances and chemical fractionation of Al, Fe, Mn, Zn, Pb, Cu and Ti in Cretaceous–Palaeocence limestones from Gubbio (Central Italy). Geochemical Journal 18, 31–41.
Calvert, S.E., Pedersen, T.F., 1993. Geochemistry of recent oxic and anoxic sediments: implications for the geological record. Marine Geology 113, 67–88.
Calvert, S.E., Piper, D.Z., 1984. Geochemistry of ferromanganese nodules: multiple diagenetic metal sources in the deep sea. Geochimica et Cosmochimica Acta 48, 1913–1928.
Calvert, S.E., Bustin, R.M., Ingall, E.D., 1996. Influence of water column anoxia and sediment supply on the burial and preservation of organic carbon in marine shales. Geochimica et Cosmochimica Acta 60, 1577–1593.
Canfield, D.E., Poulton, S.W., Knoll, A.H., Narbonne, G.M., Ross, G., Goldberg, T., Strauss, H., 2008. Ferruginous conditions dominated later Neoproterozoic deep-water chemistry. Science 321, 949–952.
Caplan, M.L., Bustin, R.M., 1999. Devonian–Carboniferous Hangenberg mass extinction event, widespread organic-rich mudrocks and anoxia: causes and consequences. Palaeogeography, Palaeoclimatology, Palaeoecology 149, 187–207.
Chen, X., Wang, C., Kuhnt, W., Holbourn, A., Huang, Y., Ma, C., 2011. Lithofacies, microfacies and depositional environments of Upper cretaceous oceanic red beds (Chuangde Formation) in southern Tibet. Sedimentary Geology 235, 100–110.
Clauer, N., Hoffert, M., Karpoff, A.M., 1982. The Rb-Sr isotope system as an index of origin and diagenetic evolution of southern Pacific red clays. Geochimica et Cosmochimica Acta 46, 2659–2664.
Conil, R., Groessens, E., Laloux, M., Poty, M., Tourneur, F., 1991. Carboniferous guide foraminifers, corals and conodonts in the Franco-Belgian and Campine Basins. CFS Courier Forschungsinstitut Senckenberg 130, 15–30.
Cruse, A.M., Lyons, T.W., 2004. Trace metal records of regional paleoenvironmental variability in Pennsylvanian (Upper Carboniferous) black shales. Chemical Geology 206, 319–345.
Cruz, M.D.R., Andreo, B., 1997. Tosudite in very low-grade metamorphic graywackes from the Malaga area (Betic Cordilleras, Spain). European Journal of Mineralogy 8, 1391–1400.
Cuven, S., Francus, P., Lamoureux, S.F., 2010. Estimation of grain size variability with micro X-ray fluorescence in laminated lacustrine sediments, Cape Bounty, Canadian High Arctic. Journal of Paleolimnology 44, 803–817.
Degtyarev, K., Yakubchuk, A.S., Luchitskaya, M.V., Tolmacheva, T.Y., Skoblenko, A.V., Tretyakov, A.A., 2021. Ordovician supra-subduction, oceanic and within-plate ocean island complexes in the Tekturmas ophiolite zone (Central Kazakhstan): age, geochemistry and tectonic implications. International Geology Review 64, 2108–2150.
Demanet, F., 1958. Contribution à l'étude du Dinantian de la Belgique. Mémoires de l'Institut Royal des Sciences Naturelles de Belgiquevol. 141 pp. 1–152 (in French with English abstract).
Dercourt, J., Zonenshain, L.P., Ricou, L.E., Kazmin, V.G., Le Pichon, X., Knipper, A.L., Grandjacquet, C., Sborshchikov, I.M., Boulin, J., Sorokhtin, O., Geyssant, J., 1985. Presentation de 9 cartes paléogéographiques au 1/20.000.000 s'étendant de l'Atlantique au Pamir pour la période du Lias à l'Actuel. Bulletin de la Société Géologique de France 8, 637–652 (in French with English abstract).
Dickson, A.J., Leng, M.J., Maslin, M.A., Röhl, U., 2010. Oceanic, atmospheric and ice-sheet forcing of South East Atlantic Ocean productivity and south African monsoon intensity during MIS-12 to 10. Quaternary Science Reviews 29, 3936–3947.
Driskill, B., Pickering, J., Rowe, H., 2018. Interpretation of High Resolution XRF Data from the Bone Spring and Upper Wolfcamp, Delaware Basin, USA. Unconventional Resources Technology Conference. American Association of Petroleum Geologists, Houston, Texas, pp. 2861–2888.
Engel, W., Feist, R., Franke, W., 1982. Le Carbonifère anté-stéphanien de la Montagne Noire: rapports entre mise en place des nappes et sedimentation. Bulletin du B.R.G. M 2, 341–389 (in French with English abstract).
Eren, M., Kadir, S., 1999. Colour origin of upper cretaceous pelagic red sediments within the Eastern Pontides, Northeast Turkey. International Journal of Earth Sciences 88, 593–595.
Fallot, P., 1948. Les Cordillères Bétiques. Estudios Geológicos 4, 83–172 (in French with English abstract).
Fang, H., Cui, Z., He, G., Huang, L., Chen, M., 2017. Phosphorus adsorption onto clay minerals and iron oxide with consideration of heterogeneous particle morphology. Science of the Total Environment 605, 357–367.
Fenchel, T., Finlay, B.J., 1995. Ecology and Evolution in Anoxic Worlds. Oxford University Press, Oxford (292 pp.).
Fike, D.A., Grotzinger, J.P., Pratt, L.M., Summons, R.E., 2006. Oxidation of the Ediacaran Ocean. Nature 444, 744–747.
Flügel, E., Herbig, H.G., 1988. Mikrofazies karbonischer Kalkgerölle aus dem Paläozoikum des Rif (Marokko): ein Beitrag zur Paläogeographie der westmediterranen Paläotethys im Karbon. Facies 19, 271–300 (in German with English abstract).
Franke, W., Paul, J., 1980. Pelagic redbeds in the Devonian of Germany—deposition and diagenesis. Sedimentary Geology 25, 231–256.
Freeman, R., Sàbat, F., Lowrie, W., Fontboté, J.M., 1989. Paleomagnetic results from Majorca (Balearic Islands, Spain). Tectonics 8, 591–608.
Gao, P., He, Z., Li, S., Lash, G.G., Li, B., Huang, B., Yan, D., 2018. Volcanic and hydrothermal activities recorded in phosphate nodules from the lower Cambrian Niutitang Formation black shales in South China. Palaeogeography, Palaeoclimatology, Palaeoecology 505, 381–397.
Gelabert, B., Fornós, J.J., Pardo, J.E., Rosselló, V.M., Segura, F., 2005. Structurally controlled drainage basin development in the south of Menorca (Western Mediterranean, Spain). Geomorphology 65, 139–155.
Glasby, G.P., 1991. Mineralogy, geochemistry, and origin of Pacific red clays: a review. New Zealand Journal of Geology and Geophysics 34, 167–176.
Gledhill, M., Buck, K.N., 2012. The organic complexation of iron in the marine environment: a review. Frontiers in Microbiology 3, 69. https://doi.org/10.3389/fmicb.2012.00069.
Goldring, R., 1962. The bathyal lull: Upper Devonian and lower Carboniferous sedimentation in the Variscan geosyncline. In: Coe, K. (Ed.), Some Aspects of the Variscan Fold Belt. Manchester University Press, Manchester, pp. 75–91.
Gómez-Gras, D., Alonso-Zarza, M., 2003. Reworked calcretes: their significance in the reconstruction of alluvial sequences (Permian–Triassic, Minorca, Balearic Islands). Sedimentary Geology 158, 299–319.

Güler, C., Thyne, G.D., McCray, J.E., Turner, A.K., 2002. Evaluation of graphical and multivariate statistical methods for classification of water chemistry data. Hydrogeology Journal 10, 455–474.
Gümbel, C.W., 1861. Geognostische Beschreibung des bayerischen Alpengebirges und seines Vorlandes. J. Perthes, Gotha (950 pp. (in German)).
Gursky, H.J., 1996. Siliceous rocks of the Culm Basin, Germany. In: Strogen, P., Sommerville, I.D., Jones, G.L. (Eds.), Recent Advances in Lower Carboniferous GeologyGeological Society of London Special Publicationvol. 107. The Geological Society, London, pp. 303–314.
Gursky, H.J., 1997. Die Kieselgesteine des Unter-Karbons im Rhenoherzynikum: Sedimentologie, Petrographie, Geochemie und Paläozeanographie. Geologische Abhandlungen Hessen 100, 1–117 (in German with English abstract).
Hahn, G., Hahn, R., Muller, P., 1997. Drevermanninae (Trilobita) aus dem Aprathium (Unter-Karbon) von Menorca (Balearen, Spanien). Geologica et Palaeontologica 31, 153–178 (in German with English abstract).
Hallam, A., 1967. Sedimentology and palaeogeographic significance of certain red limestones and associated beds in the Lias of the Alpine region. Scottish Journal of Geology 3, 195–220.
Hammer, Ø., Harper, D.A.T., Ryan, P.D., 2001. PAST: Paleontological statistics software package for education and data analysis. Palaeontologia Electronica 4, 4.. http://palaeo-electronica.org/2001_1/past/issue1_01.htm.
Hastings, D.W., Emerson, S.R., Mix, A.C., 1996. Vanadium in foraminiferal calcite as a tracer for changes in the areal extent of reducing sediments. Paleoceanography 11, 665–678.
Hay, W.W., Sibuet, J.C., Barron, E.J., Brassell, S.C., Dean, W.E., Huc, A.Y., Keating, B.H., McNulty, C.L., Meyers, P.A., Nohara, M., Schallreuter, R.E.L., Steinmetz, J.C., Stow, D. A.V., Stradner, H., Boyce, R.E., Amidei, R., 1984. Initial Reports of the Deep Sea Drilling Project75. U.S. Government Printing Office, Washington D.C, pp. 1303–pp.
He, W., Yang, Z., Du, H., Hu, J., Zhang, K., Hou, W., Li, H., 2022. Micro-mechanisms and implications of continental red beds. Minerals 12, 934. https://doi.org/10.3390/min12080934.
Hebbeln, D., Knudsen, K.L., Gyllencreutz, R., Kristensen, P., Klitgaard-Kristensen, D., Backman, J., Scheurle, C., Jiang, H., Gil, I., Smelror, M., Jones, P.D., 2006. Late Holocene coastal hydrographic and climate changes in the eastern North Sea. The Holocene 16, 987–1001.
Heij, G., Turner, B.W., Elmore, R.D., 2016. An integrated chemostratigraphic and magnetic study of the Wolfcamp Formation, Midland Basin, Texas: what can these TOOLS tell us about sequence stratigraphy and fabric anisotropy? AAPG Annual Convention and Exhibition. American Association of Petroleum Geologists, Calgary, Alberta, Canada (Search and Discovery Article #90259)
Herbig, H.G., 1985. An Upper Devonian limestone slide block near Marbella (Betic Cordillera, Southern Spain) and the palaeogeographic relations between Malaguides and Menorca. Acta Geologica Hispánica 20, 155–178.
Herbig, H.G., 1989. Carboniferous Paleogeography of the West-Mediterranean Paleotethys. Comptes Rendues du 11éme Congres International du Stratigraphie et Géologie du Carbonifèrevol. 4 pp. 186–196.
Herbig, H.G., 1994. Remarks on late Visean crinoids from the Cantabrian Mountains and Menorca (NW Spain and Balearic Islands). Revista Espanola de Paleontologia 9, 24–28.
Herbig, H.G., 1998. The late Asbian transgression in the central European Culm basins (late Viséan, cd IIIα). Zeitschrift der Deutschen Geologischen Gesellschaft 149, 39–58.
Herbig, H.G., Mamet, B., 1985. Stratigraphy of the Limestone Boulders, Marbella Formation (Betic Cordillera, Southern Spain). Compte Rendu 10e Congrès International de Stratigraphie et de Géologie du Carbonifèrevol. 1 pp. 199–212.
Herbig, H.G., Stattegger, K., 1989. Late Palaeozoic heavy minerals and clast modes from the Betic Cordillera (southern Spain): transition from a passive to an active continental margin. Sedimentary Geology 63, 93–108.
Herm, D., 1962. Die Schichten der Oberkreide (Untere, Mittlere und Obere Gosau) im Becken von Reichenhall (Bayerische/Salzburger Alpen). Zeitschrift der Deutschen Geologischen Gesellschaft 113, 320–338 (in German with English abstract).
Hikoroa, D.C.H., Crampton, J., Field, B., Schiøler, P., 2009. Upper cretaceous oceanic red beds in New Zealand. In: Hu, X., Wang, C., Scott, R.W., Wagreich, M., Jansa, L. (Eds.), Cretaceous Oceanic Red Beds: Stratigraphy, Composition, Origins, Paleoceanographic, and Paleoclimatic Significance. SEPM Special Publicationvol. 91. SEPM Society for Sedimentary Geology, Tulsa, OK, pp. 137–145.
Hild, E., Brumsack, H.J., 1998. Major and minor element geochemistry of lower Aptian sediments from the NW German Basin (core Hoheneggelsen KB 40). Cretaceous Research 19, 615–633.
Hollister, J.S., 1934. Die Stellung der Balearen im variscischen und alpinen Orogen. Abhandlungen der Gesellschaft für Wissenschaft in Göttingen, Mathematische-Physikalische Klassevol. 10 pp. 121–154 (in German).
Hu, X.M., Jansa, L., Wang, C.S., Sarti, M., Bąk, K., Wagreich, M., Michalik, J., Sotak, J., 2005. Upper cretaceous oceanic red beds (CORBs) in the Tethys: occurrences, lithofacies, age, and environments. Cretaceous Research 26, 3–20.
Hu, X., Jansa, L., Sarti, M., 2006. Mid-cretaceous oceanic red beds in the Umbria– Marche Basin, Central Italy: constraints on paleoceanography and paleoclimate. Palaeogeography, Palaeoclimatology, Palaeoecology 233, 163–186.
Hu, X., Cheng, W., Ji, J., 2009. Origin of the cretaceous oceanic red beds (CORBs) as interpreted by visible reflectance and inorganic geochemistry from the Vispi Quarry section, Central Italy. In: Hu, X., Wang, C., Scott, R.W., Wagreich, M., Jansa, L. (Eds.), Cretaceous Oceanic Red Beds: Stratigraphy, Composition, Origins and Paleoceanographic/Paleoclimatic Significance. SEPM Special Publicationvol. 91. SEPM Society for Sedimentary Geology, Tulsa, OK, pp. 183–197.
Hu, X., Scott, R.W., Cai, Y., Wang, C., Melinte-Dobrinescu, M.C., 2012. Cretaceous oceanic red beds (CORBs): different time scales and models of origin. Earth-Science Reviews 115, 217–248.
Huerta-Diaz, M.A., Morse, J.W., 1992. Pyritisation of trace metals in anoxic marine sediments. Geochimica et Cosmochimica Acta 56, 2681–2702.
Hund, F., 1966. Abhängigkeit der Farbe roter Eisen (III)-oxide von Teilchengröße und Teilchengrößenverteilung. Chemie Ingenieur Technik 38, 423–428 (in German with English abstract).
Jansa, L., Hu, X., 2009. An overview of the cretaceous pelagic black shales and red beds: Origin, paleoclimate and paleoceanographic implications. In: Hu, X., Wang, C., Scott, R.W., Wagreich, M., Jansa, L. (Eds.), Cretaceous Oceanic Red Beds: Stratigraphy, Composition, Origins and Paleoceanographic/Paleoclimatic Significance. SEPM Special Publicationvol. 91. SEPM Society for Sedimentary Geology, Tulsa, OK, pp. 59–72.
Jiang, S.Y., Jansa, L., Skupien, P., Yang, J.H., Vasicek, Z., Hu, X.M., Zhao, K.D., 2009. Geochemistry of intercalated red and gray pelagic shales from the Mazak Formation of Cenomanian age in Czech Republic. Episodes 32, 3–12.
Khorassani, M.P.K., Ghasemi-Nejad, E., Wagreich, M., Hadavi, F., Richoz, S., Harami, R.M., 2015. Biostratigraphy and geochemistry of Upper Paleocene lower Eocene Oceanic Red Beds from the Zagros Mountains. SW Iran. Journal of Earth Science and Climatic Change 6, 302. https://doi.org/10.4172/2157-7617.1000302.
Kiipli, E., Kallaste, T., Kiipli, T., 2000. Hematite and goethite in Telychian marine red beds of the East Baltic. GFF Geologiska Föreningens Förhandlingar 122, 281–286.
Kirschvink, J.L., 1980. The least-squares line and plane and the analysis of palaeomagnetic data. Geophysical Journal International 62, 699–718.
Koptíková, L., Bábek, O., Hladil, J., Kalvoda, J., Slavík, L., 2010. Stratigraphic significance and resolution of spectral reflectance logs in lower Devonian carbonates of the Barrandian area, Czech Republic; a correlation with magnetic susceptibility and gamma-ray logs. Sedimentary Geology 225, 83–98.
Korn, D., 1996. Revision of the Rhenish late Viséan goniatite stratigraphy. Annales de la Société Géologique de Belgique 117, 129–136.
Krainer, K., Vachard, D., 2015. Late Viséan (MFZ14) foraminifers and algae from the Kirchbach Limestone (Carnic Alps, Austria) and geological implications. Facies 61, 4–18.
Krenmayr, H.G., 1996. Hemipelagic and turbiditic mudstone facies associations in the Upper Cretaceous Gosau Group of the Northern Calcareous Alps (Austria). Sedimentary Geology 101, 149–172.
Kullmann, J., Schönenberg, R., 1978. Facies differentiation caused by wrench deformation along a deep-seated fault system (León Line, Cantabrian Mountains, North Spain). Tectonophysics 48, 15–22.
Kylander, M.E., Ampel, L., Wohlfarth, B., Veres, D., 2011. High-resolution X-ray fluorescence core scanning analysis of Les Echets (France) sedimentary sequence: new insights from chemical proxies. Journal of Quaternary Science 26, 109–117.
Lajoie, J., Chagnon, A., 1973. Origin of red beds in a Cambrian flysch sequence, Canadian Appalachians, Quebec. Sedimentology 20, 91–103.
Li, X., Cai, Y., 2013. Constraining the colouration mechanisms of Cretaceous Oceanic Red Beds using diffuse reflectance spectroscopy. Cretaceous Research 46, 257–266.
Li, X., Hu, X., Cai, Y., Han, Z., 2011. Quantitative analysis of iron oxide concentrations within Aptian–Albian cyclic oceanic red beds in ODP Hole 1049C, North Atlantic. Sedimentary Geology 235, 91–99.
Li, M., Song, H., Wignall, P.B., She, Z., Dai, X., Song, H., Xiao, Q., 2019. Early Triassic oceanic red beds coupled with deep sea oxidation in South Tethys. Sedimentary Geology 391, 105519. https://doi.org/10.1016/j.sedgeo.2019.105519.
Linol, B., Bercovici, A., Bourquin, S., Diez, J.B., López-Gómez, J., Broutin, J., Durand, M., Villanueva-Amadoz, U., 2009. Late Permian to Middle Triassic correlations and palaeogeographical reconstructions in south-western European basins: new sedimentological data from Minorca (Balearic Islands, Spain). Sedimentary Geology 220, 77–94.
Liu, J.B., Wang, Y., Zhang, X.L., Rong, J.Y., 2016. Early Telychian (Silurian) marine siliciclastic red beds in the Eastern Yangtze Platform, South China: distribution pattern and controlling factors. Canadian Journal of Earth Sciences 53, 712–718.
Liu, X., Hou, M., Chang, X., Wang, S., Ogg, J.G., Luo, H., Zhang, H., Mu, C., Liu, Y., 2021. Formation of late Ordovician marine red beds: a case study of Sandbian deposits in the Tarim Basin, Northwest China. Global and Planetary Change 207, 103669. https://doi.org/10.1016/j.gloplacha.2021.103669.
Luan, X.C., Wu, R.C., Zhan, R.B., Liu, J.B., 2019. The Zitai Formation in South China: unique deeper-water marine red beds in terms of lithology, distribution and δ13Ccarb chemostratigraphy. Palaeoworld 28, 198–210.
Luan, X., Zhang, X., Wu, R., Zhan, R., Liu, J., Wang, G., Zhang, Y., 2021. Environmental changes revealed by Lower–Middle Ordovician deeper-water marine red beds from the marginal Yangtze Platform, South China: links to biodiversification. Palaeogeography, Palaeoclimatology, Palaeoecology 562, 110116. https://doi.org/10.1016/j.palaeo.2020.110116.
Marsh, R., Mills, R.A., Green, D.R., Salter, I., Taylor, S., 2007. Controls on sediment geochemistry in the Crozet region. Deep Sea Research Part II: Topical Studies in Oceanography 54, 2260–2274.
Marshall, M.H., Lamb, H.F., Huws, D., Davies, S.J., Bates, R., Bloemendal, J., Boyle, J., Leng, M.J., Umer, M., Bryant, C., 2011. Late Pleistocene and Holocene drought events at Lake Tana, the source of the Blue Nile. Global and Planetary Change 78, 147–161.
Martin, K.G., Carr, T.R., 2020. Developing a quantitative mudrock calibration for a handheld energy dispersive X-ray fluorescence spectrometer. Sedimentary Geology 398, 105584. https://doi.org/10.1016/j.sedgeo.2019.105584.
Melinte, M.C., Jipa, D., 2005. Campanian–Maastrichtian red beds in the Romanian Carpathians: biostratigraphical and genetical significance. Cretaceous Research 26, 49–56.
Montero-Serrano, J.C., Palarea-Albaladejo, J., Martín-Fernández, J.A., Martínez-Santana, M., Gutiérrez-Martín, J.V., 2010. Sedimentary chemofacies characterization by means of multivariate analysis. Sedimentary Geology 228, 218–228.

Morford, J.L., Russell, A.D., Emerson, S., 2001. Trace metal evidence for changes in the redox environment associated with the transition from terrigenous clay to diatomaceous sediments, Saanich Inlet, BC. Marine Geology 174, 355–369.
Morton, A.C., Yaxley, G., 2007. Detrital apatite geochemistry and its application in provenance studies. In: Arribas, J., Critelli, S., Johnsson, M.J. (Eds.), Sedimentary Provenance and Petrogenesis: Perspectives from Petrography and GeochemistryGeological Society of America Special Papervol. 420. Geological Society of America, Boulder, Colorado, pp. 319–344.
Myrow, P., 2005. Sedimentary environments - storms and storm deposits. Encyclopedia of Geology 580–587.
Neuhuber, S., Wagreich, M., 2009. Geochemical characterization of Santonian cyclic oceanic red beds in the Alpine Tethys (Rehkogelgraben section, Austria). In: Hu, X., Wang, C., Scott, R.W., Wagreich, M., Jansa, L. (Eds.), Cretaceous Oceanic Red Beds: Stratigraphy, Composition, Origins and Paleoceanographic and Paleoclimatic Significance. SEPM Special Publicationvol. 91. SEPM Society for Sedimentary Geology, Tulsa, OK, pp. 199–207.
Neuhuber, S., Wagreich, M., Wendler, I., Spotl, C., 2007. Turonian oceanic red beds in the eastern Alps: concepts for palaeoceanographic changes in the Mediterranean Tethys. Palaeogeography, Palaeoclimatology, Palaeoecology 251, 222–238.
Nicolaus, H.J., 1963. Zur Stratigraphie und Fauna der *crenistria*-Zone im Kulm des Rheinischen Schiefergebirges. Beihefte zum Geologischen Jahrbuch 53, 1–246 (in German with English abstract).
Nizou, J., Hanebuth, T.J., Heslop, D., Schwenk, T., Palamenghi, L., Stuut, J.B., Henrich, R., 2010. The Senegal River mud belt: a high-resolution archive of paleoclimatic change and coastal evolution. Marine Geology 278, 150–164.
O'Dogherty, L., Rodríguez-Cañero, R., Gursky, H.J., Martín-Algarra, A., Caridroit, M., 2000. New data on Lower Carboniferous stratigraphy and palaeogeography of the Malaguide complex (Betic Cordillera, southern Spain). Comptes Rendus de l'Académie des Sciences de Paris 331, 1–9.
Orr, P.J., 1994. Trace fossil tiering within event beds and preservation of frozen profiles: an example from the lower Carboniferous of Menorca. Palaios 9, 202–210.
Orr, P.J., Benton, M.J., Trewin, N.H., 1996. Deep marine trace fossil assemblages from the lower Carboniferous of Menorca, Balearic Islands, western Mediterranean. Geological Journal 31, 235–258.
Ortega-Huertas, M., Monaco, P., Palomo, I., 1993. First data on clay mineral assemblages and geochemical characteristics of Toarcian Sedimentation in the umbriamarche basin (central Italy). Clay Minerals 28, 297–310.
Pedersen, T.F., Price, N.B., 1982. The geochemistry of manganese carbonate in Panama Basin sediments. Geochimica et Cosmochimica Acta 46, 59–68.
Pomar, L., Obrador, A., Westphal, H., 2002. Sub-wavebase cross-bedded grainstones on a distally steepened carbonate ramp, Upper Miocene, Menorca, Spain. Sedimentology 49, 139–169.
Préat, A., Morano, S., Loreau, J.P., Durlet, C., Mamet, B., 2006. Petrography and biosedimentology of the Rosso Ammonitico Veronese (middle-upper Jurassic, north-eastern Italy). Facies 52, 265–278.
Préat, A., De Ridder, C., Gillan, D., 2018. Bacterial origin of the red pigmentation of Phanerozoic carbonate rocks: an integrated study of geology-biology-chemistry. Geologica Belgica 21, 167–175.
Premoli Silva, I., Erba, E., Tornaghi, M.E., 1989. Paleoenvironmental Signals and Changes in Surface Fertility in Mid-Cretaceous Corgrich Pelagic Facies of the Fucoid Marls (Central Italy). Geobios Memoire Specialvol. 11 pp. 225–236.
Rajendran, A., Dileepkumar, M., Bakker, J.F., 1992. Control on manganese and iron in Skagerrak sediment (northeastern NorthSea). Chemical Geology 98, 111–129.
Raymond, D., Caridroit, M., 1994. Le Dévonien-Carbonifère inférieur du Priorat (Catalogne, Espagne): nouvelles données micropaléontologiques et interprétation paléogéographique. Acta Geologica Hispánica 28, 27–31 (in French with English abstract).
Raymond, D., Lethiers, F., 1990. Signification géodynamique de l'événement radiolaritique dinantien dans les zones externes sudvarisques (Sud de la France et Nord de l'Espagne). Comptes Rendus de l'Académie des Sciences Série II 310, 1263–1269 (in French with English abstract).
Richter, T.O., Van der Gaast, S., Koster, B., Vaars, A., Gieles, R., de Stigter, H.C., De Haas, H., van Weering, T.C., 2006. The Avaatech XRF Core Scanner: Technical Description and Applications to NE Atlantic Sediments. Geological Society of London Special Publicationsvol. 267 pp. 39–50.
Rodríguez-Perea, A., Ramos-Guerrero, E., 1984. Presencia de Paleozoico en la Sierra de Tramuntana (Mallorca). Bolletí de la Societat d'Història Natural de les Balearsvol. 28 pp. 145–148 (in Spanish with English abstract).
Rong, J.Y., Wang, Y., Zhang, X.L., 2012. Tracking shallow marine red beds through geological time as exemplified by the lower Telychian (Silurian) in the Upper Yangtze Region, South China. Science in China Series D: Earth Sciences 55, 699–713.
Rosell, J., Elizaga, E., 1989. Evolución tectosedimentaria del Paleozoico de la Isla de Menorca. Boletín Geológico y Minero 100, 193–204 (in Spanish with English abstract).
Rosell, J., Arribas, J., Elizaga, E., Gómez-Gras, D., 1988. Caracterización sedimentológica y petrográfica de la serie permo-triásica de la isla de Menorca. Boletín Geológico y Minero 99, 71–82 (in Spanish with English abstract).
Rothwell, R.G., Croudace, I.W., 2015. Twenty years of XRF core scanning marine sediments: what do geochemical proxies tell us? In: Rothwell, R.G., Croudace, I.W. (Eds.), Micro-XRF Studies of Sediment Cores: Applications of a Non-destructive Tool. Springer, Dordrecht, pp. 25–102
Rowe, H., Sivil, E., Hendrix, C., Narasimhan, S., Benson, A., Morrell, A., Torrez, G., Mainali, P., 2017. Defining Linkages Between Chemofacies and Mechanical Stratigraphy in the Austin Chalk: Implications for Geomechanics and Induced Fracture Simulations. Unconventional Resources Technology Conference. American Association of Petroleum Geologists, Austin, Texas, pp. 572–579.
Sàbat, F., Gelabert, B., Rodriguez-Perea, A., 2018. Minorca, an exotic Balearic Island (western Mediterranean). Geologica Acta 16, 411–426.
Scott, R., 2009. Chronostratigraphic database for Upper cretaceous oceanic red beds (CORBs). In: Hu, X., Wang, C., Scott, R.W., Wagreich, M., Jansa, L. (Eds.), Cretaceous Oceanic Redbeds: Stratigraphy, Composition, Origins, Paleogeographic, and Paleoclimatic Significance. SEPM Special Publicationvol. 91. SEPM Society for Sedimentary Geology, Tulsa, OK, pp. 31–53.
Shala, S., Helmens, K.F., Luoto, T.P., Väliranta, M., Weckström, J., Salonen, J.S., Kuhry, P., 2014. Evaluating environmental drivers of Holocene changes in water chemistry and aquatic biota composition at Lake Loitsana, NE Finland. Journal of Paleolimnology 52, 311–329.
Skupien, P., Bubík, M., Švábenická, L., Mikuláš, R., Vašíček, Z., Matýsek, D., 2009. Cretaceous oceanic red beds in the Outer Western Carpathians of the Czech Republic. In: Hu, X., Wang, C., Scott, R., Wagreich, M., Jansa, L. (Eds.), Cretaceous Oceanic Red Beds: Stratigraphy, Composition, Origins, and Paleoceanographic and Paleoclimatic Significance. SEPM Special Publicationvol. 91. SEPM Society for Sedimentary Geology, Tulsa, OK, pp. 99–109.
Song, H.J., Jiang, G.Q., Poulton, S.W., Wignall, P.B., Tong, J.N., Song, H.Y., An, Z.H., Chu, D.L., Tian, L., She, Z.B., Wang, C.S., 2017. The onset of widespread marine red beds and the evolution of ferruginous oceans. Nature Communications 8, 399. https://doi.org/10.1038/s41467-017-00502-x.
Spofforth, D.J., Pälike, H., Green, D., 2008. Paleogene record of elemental concentrations in sediments from the Arctic Ocean obtained by XRF analyses. Paleoceanography 23, PA1S09. https://doi.org/10.1029/2007PA001489.
Tisserand, A., Malaizé, B., Jullien, E., Zaragosi, S., Charlier, K., Grousset, F., 2009. African monsoon enhancement during the penultimate glacial period (MIS 6.5–170 ka) and its atmospheric impact. Paleoceanography 24, PA2220. https://doi.org/10.1029/2008PA001630.
Torrent, J., Schwertmann, U., 1987. Influence of hematite on the color of red beds. Journal of Sedimentary Petrology 57, 682–686.
Tribovillard, N., Algeo, T.J., Lyons, T., Riboulleau, A., 2006. Trace metals as paleoredox and paleoproductivity proxies: an update. Chemical Geology 232, 12–32.
Tucker, M.E., 2003. Sedimentary Rocks in the Field. John Wiley and Sons, Chichester (234 pp.).
Turekian, K.K., Wedepohl, K.H., 1961. Distribution of the elements in some major units of the earth's crust. Geological Society of America Bulletin 72, 175–192.
Turgeon, S., Brumsack, H.J., 2006. Anoxic vs dysoxic events reflected in sediment geochemistry during the Cenomanian–Turonian Boundary Event (Cretaceous) in the Umbria–Marche Basin of central Italy. Chemical Geology 234, 321–339.
Turner, P., 1980. Continental Red Beds. Developments in Sedimentology 29. Elsevier, Amsterdam (561 pp.).
Turner, B., 2016. Utilization of Chemostratigraphic Proxies for Generating and Refining Sequence Stratigraphic Frameworks in Mudrocks and Shales. (Ph.D. thesis)University of Oklahoma, Norman, Oklahoma (135 pp.).
Turner, B.W., Slatt, R.M., Tréanton, J.A., 2015. The Use of Chemostratigraphy to Refine Ambiguous Sequence Stratigraphic Correlations in Marine Shales: An Example from the Woodford Shale, Oklahoma. Unconventional Resources Technology Conference. American Association of Petroleum Geologists, San Antonio, Texas, pp. 19–128.
Turner, B.W., Tréanton, J.A., Slatt, R.M., 2016. The use of chemostratigraphy to refine ambiguous sequence stratigraphic correlations in marine mudrocks. An example from the Woodford Shale, Oklahoma, USA. Journal of the Geological Society 173, 854–868.
Wagreich, M., 1992. Correlation of Late Cretaceous calcareous nannofossil zones with ammonite zones and planktonic foraminifera: the Austrian Gosau sections. Cretaceous Research 13, 505–516.
Wagreich, M., Krenmayr, H.G., 1993. Nannofossil biostratigraphy of the Late Cretaceous Nierental Formation, Northern Calcareous Alps (Bavaria, Austria). Zitteliana 20, 67–77.
Wagreich, M., Krenmayr, H.G., 2005. Upper Cretaceous oceanic red beds (CORB) in the Northern Calcareous Alps (Nierental Formation, Austria): slope topography and clastic input as primary controlling factors. Cretaceous Research 26, 57–64.
Wagreich, M., Neuhuber, S., Egger, H., Wendler, I., Scott, R.W., Malata, E., Sanders, D., 2009. Cretaceous Oceanic Red Beds (CORBs) in the Austrian Eastern Alps: passive margin vs. active-margin depositional settings. In: Hu, X., Wang, C., Scott, R.W., Wagreich, M., Jansa, L. (Eds.), Cretaceous Oceanic Red Beds: Stratigraphy, Composition, Origins and Paleoceanographic and Paleoclimatic Significance. SEPM Special Publicationvol. 91. SEPM Society for Sedimentary Geology, Tulsa, OK, pp. 73–88.
Wajsprych, B., Achramowicz, S., 2003. On the new wildflysch-to-flysch, blueschist-rich lower Visean succession of the Western Sudetes (SW Poland). Annales. Societatis Geologorum Poloniae 73, 123–137.
Wang, C., Huang, Y., Hu, X., Li, X., 2004. Cretaceous oceanic redbeds: implications for paleoclimatology and paleoceanography. Acta Geologica Sinica—English Edition 78, 873–877.
Wang, C., Hu, X.M., Sarti, M., Scott, R.W., Li, X.H., 2005. Upper cretaceous oceanic red beds in southern Tibet: a major change from anoxic to oxic, deep-sea environments. Cretaceous Research 26, 21–32.
Wang, C., Hu, X., Huang, Y., Scott, R., Wagreich, M., 2009. Cretaceous oceanic red beds (CORB): a window on global oceanic/climatic change. In: Hu, X., Wang, C., Scott, R. W., Wagreich, M., Jansa, L. (Eds.), Cretaceous Oceanic Red Beds: Stratigraphy, Composition, Origins and Paleoceanographic/Paleoclimatic Significance. SEPM Special Publicationvol. 91. SEPM Society for Sedimentary Geology, Tulsa, OK, pp. 13–33.
Wang, C., Hu, X., Huang, Y., Wagreich, M., Scott, R.W., Hay, W.W., 2011. Cretaceous oceanic red beds as possible consequence of oceanic anoxic events. Sedimentary Geology 235, 27–37.
Ward Jr., J.H., 1963. Hierarchical grouping to optimize an objective function. Journal of the American Statistical Association 58, 236–244.

Wedepohl, K.H., 1971. Environmental influences on the chemical composition of shales and clays. In: Ahrens, L.H., Press, F., Runcorn, S.K., Urey, H.C. (Eds.), Physics and Chemistry of the Earth. Pergamon, Oxford, pp. 305–333.
Wedepohl, K.H., 1995. The composition of the continental crust. Geochimica et Cosmochimica Acta 59, 1217–1232.
Wehrly, B., Stumm, W., 1989. Vanadyl in natural waters: adsorption, and hydrolysis promote oxygenation. Geochimica et Cosmochimica Acta 53, 69–77.
Wilhelm, B., Arnaud, F., Sabatier, P., Magand, O., Chapron, E., Courp, T., Tachikawa, K., Fanget, B., Malet, E., Pignol, C., Bard, E., 2013. Palaeoflood activity and climate change over the last 1400 years recorded by lake sediments in the north-west European Alps. Journal of Quaternary Science 28, 189–199.
Yilmaz, I.O., 2008. Cretaceous pelagic red beds and black shales (Aptian–Santonian), NW Turkey: global oceanic anoxic and oxic events. Turkish Journal of Earth Sciences 17, 263–296.
Zaragosi, S., Bourillet, J.F., Eynaud, F., Toucanne, S., Denhard, B., Van Toer, A., Lanfumey, V., 2006. The impact of the last European deglaciation on the deep-sea turbidite systems of the Celtic-Armorican margin (Bay of Biscay). Geo-Marine Letters 26, 317–329.
Zhang, X.L., Wang, Y., Rong, J.Y., Li, R.Y., 2014. Pigmentation of the early Silurian shallow marine red beds in South China as exemplified by the Rongxi Formation of Xiushan, southeastern Chongqing, Central China. Palaeoworld 23, 240–251.
Ziegler, A., McKerrow, W., 1975. Silurian marine red beds. American Journal of Science 275, 31–56.
Ziegler, M., Jilbert, T., de Lange, G.J., Lourens, L.J., Reichart, G.J., 2008. Bromine counts from XRF scanning as an estimate of the marine organic carbon content of sediment cores. Geochemistry, Geophysics, Geosystems 9, Q05009. https://doi.org/10.1029/2007GC001932.